Chapter 7

Valley Polarized Single Photon Source Based on Transition Metal Dichalcogenides Quantum Dots

Fanyao Qu, Alexandre Cavalheiro Dias, Antonio Luciano de Almeida Fonseca, Marco Cezar Barbosa Fernandes and Xiangmu Kong

Additional information is available at the end of the chapter

http://dx.doi.org/10.5772/intechopen.70300

Abstract

Photonic quantum computer, quantum communication, quantum metrology, and optical quantum information processing require a development of efficient solid-state single photon sources. However, it still remains a challenge. We report theoretical framework and experimental development on a novel kind of valley-polarized single-photon emitter (SPE) based on two-dimensional transition metal dichalcogenides (TMDCs) quantum dots. In order to reveal the principle of the SPE, we make a brief review on the electronic structure of the TMDCs and excitonic behavior in photoluminescence (PL) and in magneto-PL of these materials. We also discuss coupled spin and valley physics, valley-polarized optical absorption, and magneto-optical absorption in TMDC quantum dots. We demonstrate that the valley-polarization is robust against dot size and magnetic field, but optical transition energies show sizable size-effect. Three versatile models, including density functional theory, tight-binding and effective $k \cdot p$ method, have been adopted in our calculations and the corresponding results have been presented.

Keywords: single-photon source, quantum dots, transition metal dichalcogenides

1. Introduction

Traditional semiconductors have been used for decades for making all sorts of devices like diodes, transistors, light emitting diodes, and lasers [1]. Due to the advances of technology in fabrication, it is possible not only to make ever pure semiconductor crystals, but also to study heterostructures, in which carriers (electrons or holes) are confined in thin sheets, narrow lines, or even a point [1, 2]. Quantum dots (QDs) are zero-dimensional objects where all the three

spatial dimensions are quantized with sizes smaller than some specific characteristic lengths, e.g., the exciton Bohr radius [1, 2]. Because of confinement, electrons in the QDs occupy discrete energy levels, in a similar way as they do in atoms [2, 3]. For these reasons, QDs are also referred to as artificial atoms [1, 2]. In spite of some similarities between the QD and the real atom, the former demonstrates several special characteristics. For instance, its size can vary from a few to hundreds of nanometers, and it can trap from a very small number of electrons ($Ne < 10$) to $50 - 100$ electrons or more [1]. In addition, the shape of the QD that can be tuned at will determine its spatial symmetry. In turn, the change in spatial symmetry modifies physical properties of the system. As known, the three-dimensional spherically symmetric QDs possess degenerate electron shells, 1*s*, 2*s*, 2*p*, 3*s*, 3*p*,… [3]. When the number of electrons is equal to 2, 10, 18, 36,…, the electron shells are completely filled [1], yielding a particularly stable configuration. In contrast, a two-dimensional cylindrically symmetric parabolic potential leads to formation of a two-dimensional shell structure with the magic numbers 2, 6, 12, 20,…[2, 4, 5]. Hence, the lower degree of symmetry in two-dimensional QDs leads to a smaller magic number sequence. Since the shape and size of the QDs can be precisely manufactured, the energy structure of the carriers in the QDs as well as their optical, transport, magnetic, and thermal properties can be engineered in a large scale [1–9].

Various techniques have been developed to produce the QDs such as etching, regrowth from quantum well structures, beam epitaxy, lithography, holograph patterning, chemical synthesis, etc [1, 2]. Consequently, many kinds of QDs emerge. According to the electrical property of their parent material, they can be classified into metal, semiconductor, or super-conducting dots. From geometry point of view, the QDs form two groups: two-dimensional [2, 4, 5, 8] or three-dimensional (3D) [1] dots. The former can be further divided into conventional 2D semiconductor QDs, such as self-assembled- and gated-QDs based on traditional semiconductor quantum wells [4–8, 10], and the novel QDs made from two-dimensional-layered materials (2DLMs) [11–15].

Atomically thin 2DLMs have revolutionized nanoscale materials science [16]. The interatomic interaction within layers is covalent in nature, while the layers are held together by weak van der Waals (vdW) forces. The family of 2D materials, which started with graphene [16], has expanded rapidly over the past few years and now includes insulators, semiconductors, semimetals, metals, and superconductors [17–19]. The most well studied 2D systems beyond graphene, are the silicene, germanene, stanine, and borophene, organic-inorganic hybrid perovskites, insulator hexagonal boron-nitride [17, 18], the anisotropic semiconductor phosphorene, transition metal-carbides, -nitrides, -oxides, and -halides, as well as the transition metal dichalcogenides (TMDCs) [20–28]. Compared with traditional semiconducting materials, the 2DLMs take advantage of inherent flexibility and an atomically-thin geometry. Moreover, because of their free dangling bonds at interfaces [25, 29, 30], two-dimensional-layered materials can easily be integrated with various substrates [17]. They can also be fabricated in complex-sandwiched structures or even suspended to avoid the influence of the substrate [31]. The monolayer TMDCs with infinite geometry exhibit strong carrier confinement in one dimension but preserve the bulk-like dispersion in the 2D plane. In contrast, electrons in a TMDC QD are restricted in three dimensions, which present size tunable electronic and optical properties in addition to the remarkable

http://dx.doi.org/10.5772/intechopen.70300

characteristics related to spin-valley degree of freedom inherited from its 2D bulk materials. Very recently, graphene QDs (GQDs) have attracted intensive research interest due to their high transparency and high surface area. Many remarkable applications ranging from energy conversion to display to biomedicine are prospected [11]. Nevertheless, from quantum nano-devices point of view, the TMDCs have advantages over graphene. For instance, the semiconducting TMDCs have a band gap large enough to form a QD using the electric field, as shown in **Figure 1**, unlike etched GQDs made on semi-metallic graphene.

The applications of quantum dots are still mostly restricted to research laboratories, but they are remarkable due to the fact that QDs provide access to the quantum mechanical degrees of freedom of few carriers. Single electron transistors [1–6], the manipulation of one [4–7] or two [1–3] electron spins, manipulation of a single spin in a single magnetic ion-doped QD [4–7] are only some examples. Optically active quantum dots can also be used in both quantum communication and quantum computation [4–7, 12–15]. The emerging field of quantum information technology, as unconditionally quantum cryptography, quantum-photonic communication and computation, needs the development of individual photon sources [12–15, 32, 33]. Recently, individual photon emitters based on defects in TMDC monolayers with different sample types (WSe_2 and $MoSe_2$) have been reported, but only operate at cryogenic temperatures [12, 13, 32–35]. In addition, it should be kept in mind that the presence of defects is not always beneficial for the PL signal. For instance, defect-mediated nonradiative recombination might result in an internal quantum yield droop in the defective TMDCs [26–28]. In this context, single quantum emitter based on QD is desirable [14, 15].

In this chapter, we show the optical and magneto-optical properties of the TMDC QD's. We choose MoS_2, which has been widely studied in the literature as our example. Three versatile models including density functional theory, tight-binding, and effective $k \cdot p$ approach have been adopted in our calculations and the corresponding results have been presented. We show that the valley-polarization is robust against dot size and magnetic field, but the optical transition energies show sizable size effect. Based on the computed optical absorption spectra, a novel kind of valley-polarized single-photon source based on TMDC quantum dot is proposed [15].

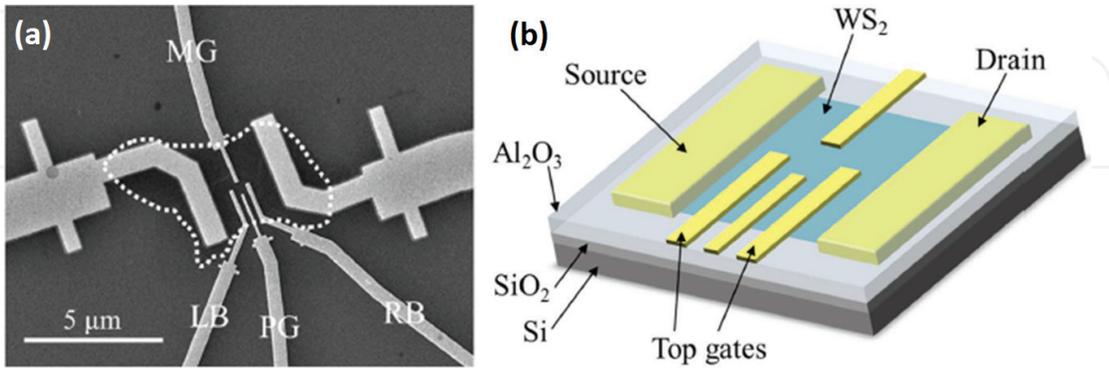

Figure 1. (a) Scanning electron microscope image of the WS_2 quantum dot studied. The WS_2 flake is highlighted by the white dotted line, and the four top gates are labeled as MG, LB, PG, RB. The scale bar represents 5 μ m. (b) Three-dimensional schematic view of the device [20]. (Copyright 2015 by the Royal Society of Chemistry. Reprinted with permission).

2. Physical properties of transition metal dichalcogenides

2.1. Electronic band structure of transition metal dichalcogenides

Layered TMDCs have the generic formula MX_2, where M stands for a metal and X represents a chalcogen. The monolayer crystal structure of the MoS_2, which is one of the most studied TMDCs in the literature is shown in **Figure 2**. Notice that the monolayer MoS_2 has a trigonal prism crystal structure. An inversion asymmetry results in a large direct gap semiconductor with the gap lying at the two inequivalent *K*-points of the hexagonal Brillouin zone.

The major orbital contribution at the edge of the conduction band (CB) is from $d_{3z^2-r^2}$ orbital of the metal, plus minor contributions from p_x, and p_y orbitals of chalcogens. On the other hand, at the edge of the valence band (VB) at the *K*-point, the most important orbital contribution is due to a combination of d_{xy} and $d_{x^2-y^2}$ of the metal, which hybridize to p_x and p_y orbitals of the chalcogen atoms [24]. In addition, there is a strong spin-orbit interaction (SOI), especially in the valence band. The spatial inversion asymmetry along with strong SOI leads to a spin-valley coupling, which results in the spin of electron being locked to the valley [20, 21, 36], as demonstrated in **Figure 3(a)**. Furthermore, the band structure in the *K*-valley presents time reversal symmetry with that in *K*′-valley. And, it changes dramatically as the number of the layers of the TMDC increases. When the thickness increases, the band gap in MoS_2 and other group VI TMDCs decreases, and more importantly, the material becomes an indirect gap semiconductor [37], as shown in **Figure 3(b)**.

In order to get insight into the physical origins of the band gap variations with the number of layers, **Figure 4** shows evolutions of the band gaps (a) and band edges (b) of MoS_2 as a function of the number of layers. Notice that with increasing layer thickness, the indirect band gap (Γ–K, Γ–Λ) becomes smaller, while the direct excitonic transition (K–K) only slightly changes, as illustrated in **Figure 4(a)**. Note also that the monolayer ($n = 1$) MoS_2 is a direct band gap semiconductor, but it becomes an indirect band gap semiconductor when the number of layers is larger than one. This phase transition is also clearly demonstrated in **Figure 4(b)**. In addition, as the number of layers increases, both the VB and CB edges at *K*-valley exhibit only slight variation while the degeneracy at Γ is lifted and a splitting of the bands occurs, which

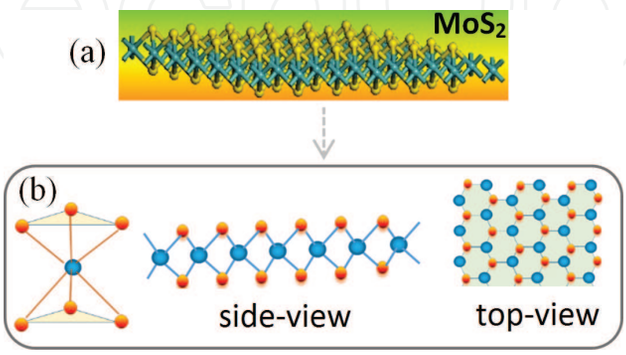

Figure 2. (a) Schematic diagram of crystal structure of MoS_2. (b) Coordination environment of Mo (blue sphere) in the structure (the left panel); the middle and the right panels correspond to side- and top- views of the monolayer MoS_2 lattice. Sulfur is shown as golden spheres.

http://dx.doi.org/10.5772/intechopen.70300

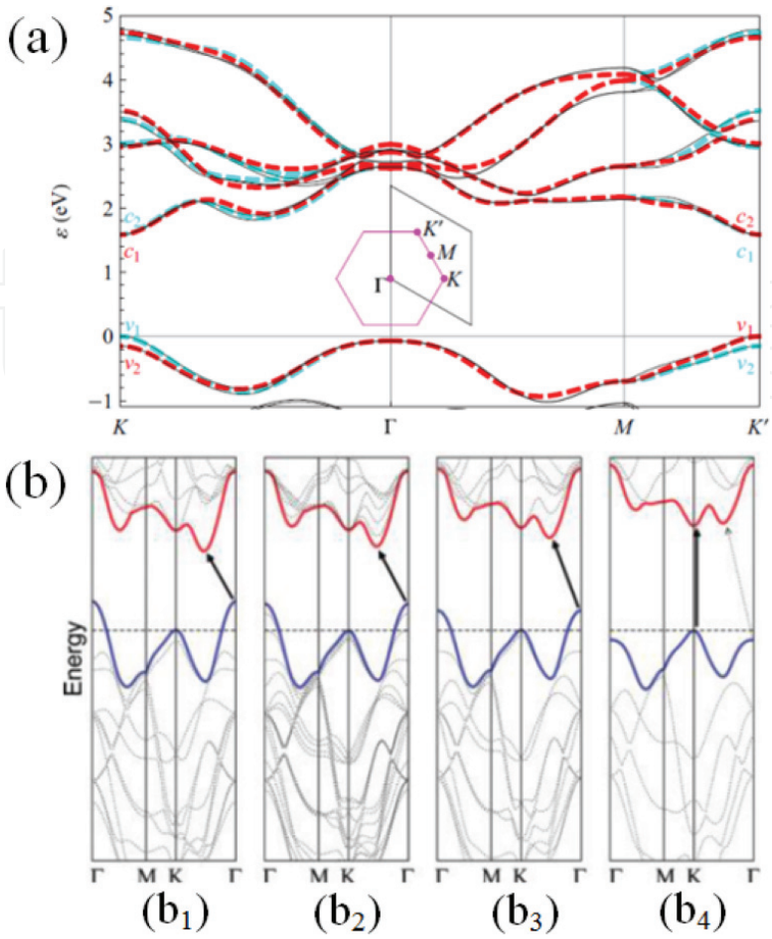

Figure 3. (a) Band structure of monolayer MoS_2. The solid curves were obtained using the QUANTUM ESPRESSO package with fully relativistic pseudopotentials under the Perdew-Burke-Ernzerhof generalized-gradient approximation, and a $16 \times 16 \times 1$ k grid. The dashed curves were calculated from the tight-binding model, with cyan (red) representing states that are even (odd) under mirror operation with respect to the Mo plane. $v_{1,2}$ and $c_{1,2}$ label the bands close to the valence and conduction band edges near the K- and K'-points. The inset shows the hexagonal Brillouin zone (pink) associated with the triangular Bravais lattice of MoS_2 and an alternate rhombohedral primitive zone (black), and labels the principle high-symmetry points in reciprocal space [36] (Copyright 2015 by American Physical Society, Reprinted with permission). (b) Calculated band structures of (b1) bulk MoS_2, (b2) quadrilayer MoS_2, (b3) bilayer MoS_2, and (b4) monolayer MoS_2. The solid arrows indicate the lowest energy transitions. Bulk MoS_2 is characterized by an indirect bandgap. The direct excitonic transition occurs at K point with a higher transition energy than that of indirect one [30]. (Copyright 2010 by the American Chemical Society. Reprinted with permission).

pushes the VB maximum to higher energy. The variation of the band gap is largely driven by the variation of the VB at Γ point. Going from a monolayer to a bilayer significantly raises the VB at Γ, resulting in a transition from the direct K–K gap to an indirect Γ–K gap. This dramatic change of electronic structure in monolayer MoS_2 results in the jump in monolayer photoluminescence efficiency.

2.1.1. Massive Dirac fermions

To gain insight of physics around the K- and K'-points, one can reduce multi-band tight-binding model to a two band **k.p** model, using Löwdin partitioning method [38]. For the monolayer TMDCs, one gets the Hamiltonian in the first order of k approximation,

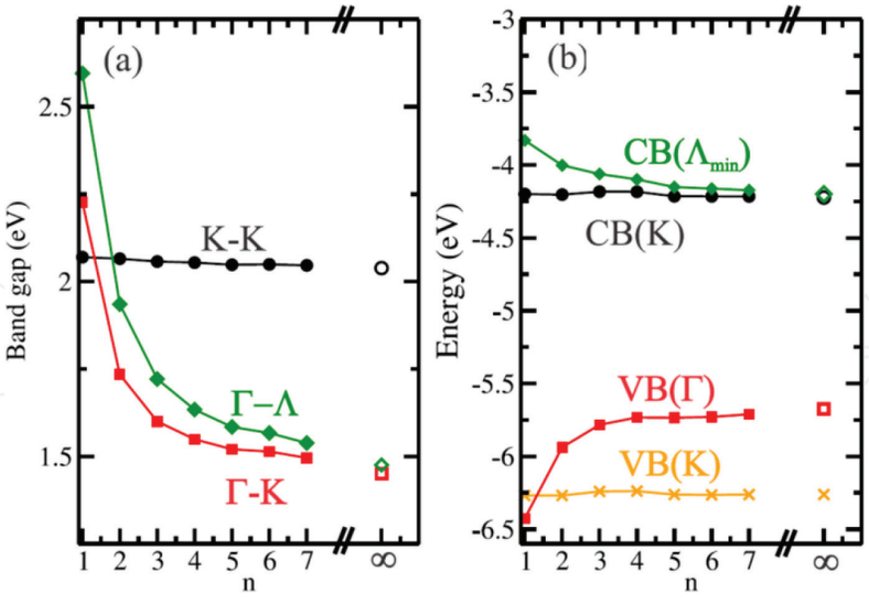

Figure 4. (a) Evolution of the band gaps as a function of the number of layers (n). The black circles $(K-K)$, red squares $(\Gamma–K)$, and green diamonds $(\Gamma–\Lambda)$ indicate the magnitude of the different band gaps. Hollow symbols indicate the bulk band gaps. (b) Position of the band edge with respect to the vacuum level for the VB at the *K*-point (orange crosses), VB at Γ(red squares), CB at the *K*-point (black circles), and CB at Λ (green diamonds) [29]. (Copyright 2014 by the American Physical Society. Reprinted with permission).

$$H(\mathbf{k},\tau,s)=\begin{pmatrix}\Delta/2 & at(\tau k_x-ik_y)\\ at(\tau k_x+ik_y) & -\Delta/2+\tau s\lambda\end{pmatrix} \tag{1}$$

where $\Delta=1.6\,eV$ is the band gap, $t=1.1\,eV$ is the effective hopping parameter, $\lambda=0.075\,eV$ is the SOI parameter, $a=3.19\,\mathring{A}$ is the lattice parameter [39], $\tau=\pm1$ is the valley index. The eigenvalues and eigenvectors can be derived straightforwardly as follows:

$$E_{\pm}(k_x,\ k_y)=\frac{\tau\lambda s}{2}\pm\sqrt{\frac{(\Delta-\lambda\tau s)^2}{4}+t^2a^2(k_x^2+k_y^2)} \tag{2}$$

and

$$\begin{aligned}|c,\ \vec{k}\ \tau,\ s_z\rangle&=|s_z\rangle\otimes\begin{pmatrix}cos\left(\frac{\vartheta_n}{2}\right)\\ \tau sin\left(\frac{\vartheta_n}{2}\right)e^{i\tau\phi_{\vec{k}}}\end{pmatrix}\\ |v,\ \vec{k}\ \tau,\ s_z\rangle&=|s_z\rangle\otimes\begin{pmatrix}-\tau sin\left(\frac{\vartheta_n}{2}\right)e^{-i\tau\phi_{\vec{k}}}\\ cos\left(\frac{\vartheta_n}{2}\right)\end{pmatrix}\end{aligned} \tag{3}$$

$$cos\vartheta_n=\frac{\Delta+(-1)^n\lambda_{so}}{2\sqrt{(\Delta+(-1)^n\lambda_{so})^2+4t^2a^2k^2}} \tag{4}$$

http://dx.doi.org/10.5772/intechopen.70300

$$tan(\phi_{\vec{k}}) = \frac{k_y}{k_x} \tag{5}$$

The energy dispersion around the K- and K'- points, described by Eq. 2, is shown in **Figure 5**. In order to see the reliability of the $\boldsymbol{k} \cdot \boldsymbol{p}$ approach, **Figure 6** plots the energy spectrum of

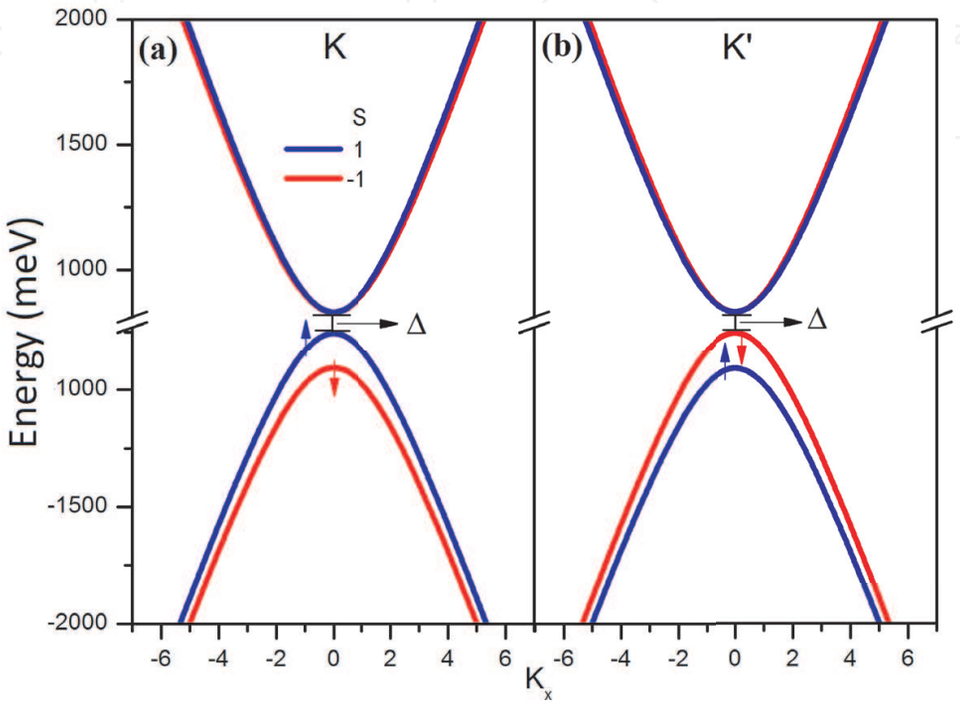

Figure 5. Energy dispersion in (a) K-valley and (b) K'-valley obtained by the $\mathbf{k} \cdot \mathbf{p}$ model.

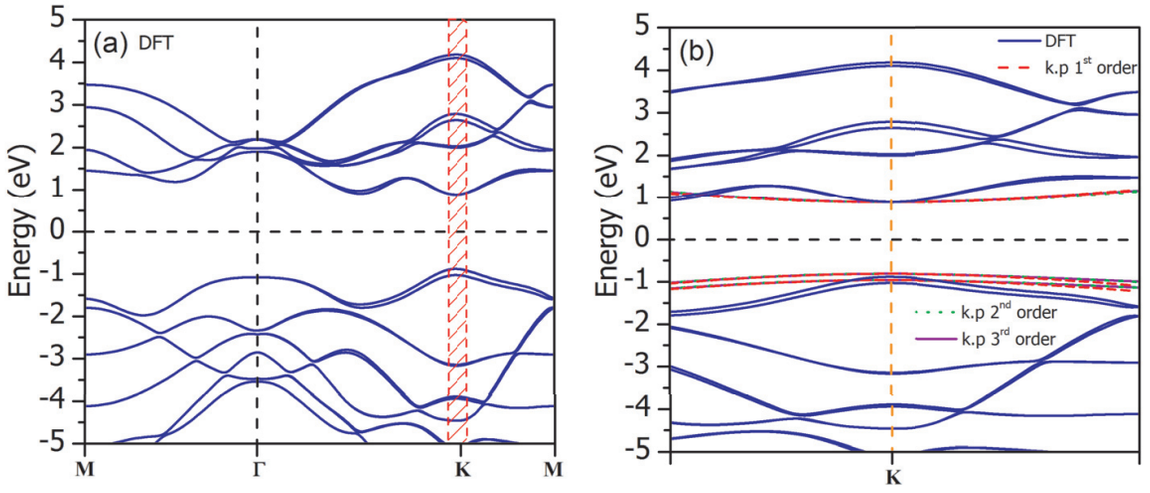

Figure 6. (a) Quasiparticle band structure of monolayer MoS_2 calculated by the density functional theory (DFT). (b) A blowup of the rectangular red area in (a). The blue (solid), red (dashed), green (dotted), and purple (dot-dashed) curves correspond to the results obtained by the DFT, and $\mathbf{k} \cdot \mathbf{p}$ theory of the first order, second order, and third order, respectively. Notice that around the K-point, all methods give almost identical results.

monolayer MoS_2 calculated by the first principle and $\boldsymbol{k}\cdot\boldsymbol{p}$ model. It can be found that in the vicinity of the K–(K')–point, they have very good agreement.

2.1.2. Landau levels of monolayer MoS_2

For a perpendicular magnetic field applied to the MoS_2 sheet, we use Peierls substitution $K_i \to \Pi_i = K_i + (e/\hbar)A_i$, where e is the elementary charge. In the Landau Gauge $\vec{A} = (0, Bx)$, we define the operators $\Pi_\pm = \tau\Pi_x \pm i\Pi_y$, which have the following properties:

$$[\Pi_-, \Pi_+] = \left(2\tau/l_B^2\right) \tag{6}$$

where the magnetic length is $l_B = \sqrt{\hbar/eB} \approx \left(25.6/\sqrt{B}\right)$. Using these operators, the destruction and creation operators are introduced in the following way:

$$\hat{b} = \left(l_B/\sqrt{2}\right)\Pi_-,$$

$$\hat{b}^\dagger = \left(l_B/\sqrt{2}\right)\Pi_+ \tag{7}$$

in the K-($\tau = 1$) valley, and

$$\hat{b} = \left(l_B/\sqrt{2}\right)\Pi_+,$$

$$\hat{b}^\dagger = \left(l_B/\sqrt{2}\right)\Pi_-. \tag{8}$$

in the K' ($\tau = -1$) valley. Then, the Hamiltonian in the presence of a perpendicular magnetic field can be well described by

$$\mathrm{H}^{\tau=1} = \begin{pmatrix} \frac{\Delta}{2} & ta\left(\sqrt{2}/l_B\right)\hat{b} \\ ta\left(\sqrt{2}/l_B\right)\hat{b}^\dagger & -\frac{\Delta}{2} + s\lambda \end{pmatrix}, \tag{9}$$

$$\mathrm{H}^{\tau=-1} = \begin{pmatrix} \frac{\Delta}{2} & ta\left(\sqrt{2}/l_B\right)\hat{b}^\dagger \\ ta\left(\sqrt{2}/l_B\right)\hat{b} & -\frac{\Delta}{2} - s\lambda \end{pmatrix}. \tag{10}$$

It is worth to mention that since the Zeeman effect is vanishingly small ($< 5\,meV$), it is neglected. After some algebra calculations, the Landau levels are obtained as follows:

$$E_\pm(\omega_c, n) = \frac{\lambda\tau s}{2} \pm \sqrt{\frac{(\Delta - \lambda\tau s)^2}{4} + t^2a^2\omega_c^2 n} \tag{11}$$

where n is an integer and $n \geq 1$, $\omega_c = \sqrt{2}/l_B$. The corresponding Landau fan diagrams of the monolayer MoS_2 are shown in **Figure 7**. The corresponding eigenfunctions are given by

http://dx.doi.org/10.5772/intechopen.70300

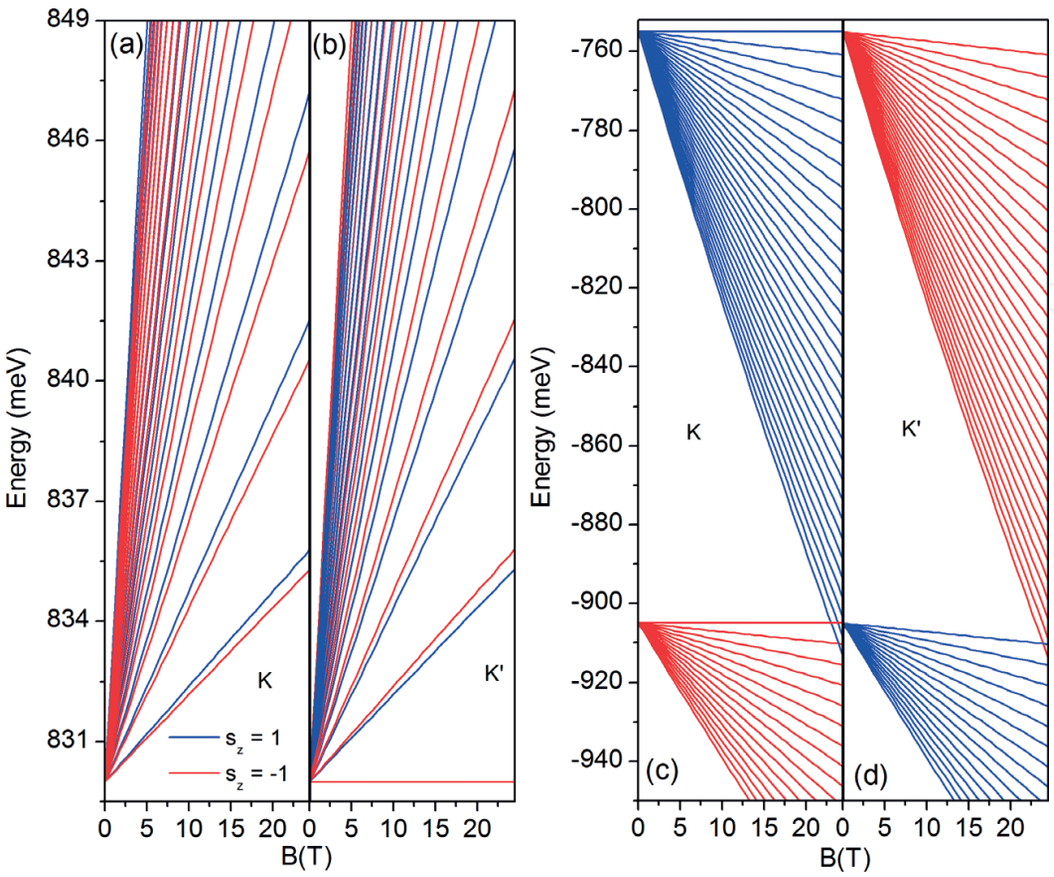

Figure 7. Conduction band Landau levels of monolayer MoS_2 in the vicinity of *K*- (a) and *K′*- (b) valleys with spin-orbit interaction (SOI). (c) and (d) are the same as (a) and (b), but for the valence band. The blue and red lines correspond to the spin-up and spin-down Landau levels, respectively.

$$\Psi_{n,\pm}^{\tau=1} = \frac{1}{N_{\tau=1}^{n}} \begin{pmatrix} -\alpha_{\lambda,s,\pm}^{n}\phi_{n-1} \\ \phi_n \end{pmatrix} \tag{12}$$

and

$$\Psi_{n,\pm}^{\tau=-1} = \frac{1}{N_{\tau=-1}^{n}} \begin{pmatrix} \phi_n \\ -\beta_{\lambda,s,\pm}^{n}\phi_{n-1} \end{pmatrix}, \tag{13}$$

where

$$\alpha_{\lambda,s,\pm}^{n} = \frac{ta\left(\sqrt{2}/l_B\right)\sqrt{n}}{\Delta/2 - E_{\pm}}, \tag{14}$$

$$\beta_{\lambda,s,\pm}^{n} = \frac{ta\left(\sqrt{2}/l_B\right)\sqrt{n}}{(-\Delta/2 - \lambda s) - E_{\pm}}, \tag{15}$$

$$N_{\tau=1}^{n,\pm} = \sqrt{(\alpha_{\lambda_{so},s_z,\pm}^{n})^2 + 1}, \tag{16}$$

$$N_{\tau=-1}^{n,\pm} = \sqrt{\left(\beta_{\lambda_{so},s_z,\pm}^{n}\right)^2 + 1}, \tag{17}$$

$$\phi_n = \sqrt{\frac{1}{2^n n!}}\left(\frac{m\omega}{\pi\hbar}\right)^{1/4} e^{-m\omega r^2/2\hbar} H_n\left(\sqrt{\frac{m\omega}{\hbar}}r\right), \tag{18}$$

$$H_n(x) = (-1)^n e^{x^2}\frac{d^n}{dx^n}e^{-x^2}. \tag{19}$$

The eigenfunctions can be written in a compact form as,

$$\Psi_{n,\pm}^{\tau} = \frac{1}{N_{\tau}^{n,\pm}}\begin{pmatrix} c_{1,n}^{\tau,\pm}\phi_{n-\left(\frac{\tau+1}{2}\right)} \\ c_{2,n,\pm}^{\tau}\phi_{n-\left(\frac{1-\tau}{2}\right)} \end{pmatrix}. \tag{20}$$

For the special case in which $n = 0$, the eigenvalues become

$$E_{n=0}^{\tau=1} = -\frac{\Delta}{2} + \lambda_{so}s_z, \tag{21}$$

$$E_{n=0}^{\tau=-1} = \frac{\Delta}{2} \tag{22}$$

and corresponding eigenfunctions turn out to be

$$\Psi_0^{\tau=1} = \begin{pmatrix} 0 \\ \phi_0 \end{pmatrix}, \tag{23}$$

$$\Psi_0^{\tau=-1} = \begin{pmatrix} \phi_0 \\ 0 \end{pmatrix}. \tag{24}$$

2.2. Optical selection rules

In monolayer TMDCs, both the top of valence bands and the bottom of conduction bands are constructed primarily by the *d*-orbits of the transition metal atoms. The giant spin-orbit coupling splits the valence bands around the K (K') valley by 0.5 eV, for MoS_2 while the conduction band splitting is neglectable. In addition, time reversal symmetry (TRS) leads to the opposite spin splitting at the K- and K'-valleys. Namely the Kramers doublet (K,↑) and (K',↓) are separated from the other doublet (K',↑) and (K, ↓) by the spin–orbit interaction (SOI) splitting, as shown in **Figure 8**.

We assume that the monolayer TMDCs are exposed to light fields with the energy $\hbar\omega$ and wave vector $k_{l,}$ which is orthogonal to the monolayer plane and much smaller than $1/a$. Up to the first order approximation, the light-matter interaction Hamiltonian is described by,

$$\mathcal{H}_{L-M} = e\mathbf{v}\cdot\mathbf{A}_{in}, \tag{25}$$

with the light field $\mathbf{A}_{in} = A_0\hat{\alpha}\cos\left(\mathbf{k}_l\cdot\mathbf{r} - \omega t\right)$ and $\mathbf{v} = (1/\hbar)\nabla_{\mathbf{k}}\mathcal{H}$ being propagation velocity [15]. Here, A_0 and $\hat{\alpha}$ stand for the amplitude and orientation of the polarization field,

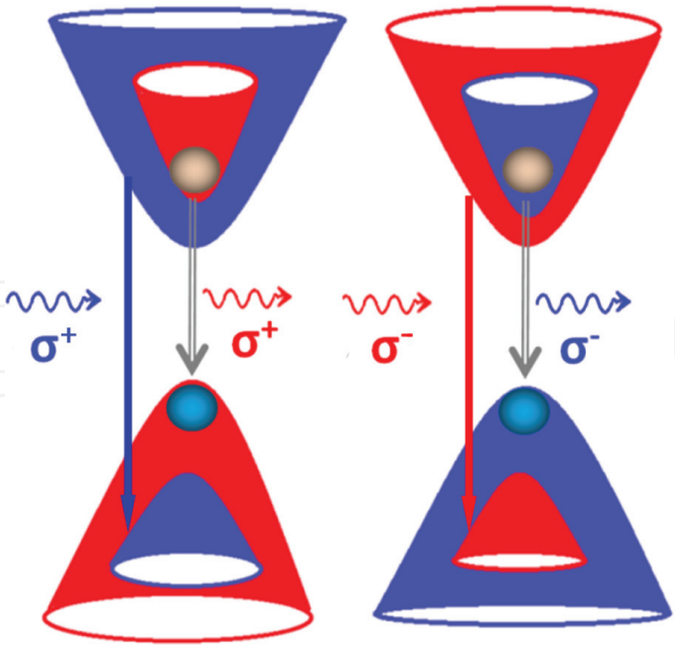

Figure 8. Schematic illustration of optical transition rules of the valley and spin in the K- (the left) and K'- (the right) valleys. The red (blue) color represents spin-up (down) states.

respectively. For an electron being excited by an incident photon from its initial state $|i\rangle$ to a final state $|f\rangle$, the transition probability is given by the Fermi's golden rule as, $W_{fi} = 2\pi/\hbar|\langle f|\mathcal{H}_{L-M}|i\rangle|^2 n(E)$, where $n(E)$ is the density of states available for the final state. Since the absorption intensity I is proportional to the transition rate, it can be evaluated by,

$$I = \sum_{m_c,\, m_v,\, n_c,\, n_v} |<\mathbf{\Psi}_c|\mathcal{H}_{L-M}|\mathbf{\Psi}_v>|^2 \Lambda\Upsilon, \tag{26}$$

where $\mathbf{\Psi}_c$ ($\mathbf{\Psi}_v$) is the conduction (valence) band wave function, $\Lambda = \gamma/\pi\{[\omega - (E_c(m_c, n_c) - E_v(m_v, n_v))]^2 + \gamma^2\}$, and $\Upsilon = f_c - f_v$, with f_i Fermi-Dirac distribution function, n_i the principal quantum number, m_i the quantum number associating with orbital angular momentum, $i = c$, and v referring to conduction and valence band, respectively, $m_c = m$ and $m_v = m'$, γ a parameter determined by the Lorentzian distribution.

For a circularly polarized (CP) light, $\hat{\alpha} = (1, \cos(\omega t - \sigma\pi/2), 0)^{\mathrm{T}}$, with $\sigma = \pm 1$ denoting the corresponding positive and negative helicities and T stands for the transpose of a matrix, then the perturbed Hamiltonian becomes,

$$\mathcal{H}_{L-M} = e^{i\omega t}\hat{W}_\sigma{}^\dagger + e^{-i\omega t}\hat{W}_\sigma, \tag{27}$$

with $\hat{W}_\sigma = etaA_0(\tau\sigma_x + i\sigma\sigma_y)/2\hbar$. For example, for $\tau = 1$, $s_z = \pm 1$, the transition rate for the monolayer TMDCs is determined by,

$$\langle c,\ \vec{k}\ |\mathrm{H}_{L-M}^{CP,+}|v,\ \vec{k}\ \rangle = \frac{2m_0 at}{\hbar}\,\delta_{s_{zv}, s_{zc}}(sin\phi_{\vec{k}} + cos\phi_{\vec{k}} cos\vartheta_n) \tag{28}$$

and

$$\langle c, \vec{k} | \mathrm{H}_{L-M}^{CP,-} | v, \vec{k} \rangle = 0 \tag{29}$$

The optical transition rate for $\tau = -1$ and $s_z = \pm 1$ can be obtained by replacing $+$ with $-$in the H_{L-M}. From Eqs. (29) and (30), notice that under CP light excitation, a valley and spin polarized emission or absorption light is expected in monolayer MoS_2, as shown in **Figure 8**. In contrast, linearly polarized light does not present valley-selected emission and absorption spectra because both *K*- and *K′*- valleys absorb light simultaneously.

2.3. Valley polarized photoluminescence and excitonic effects of the monolayer TMDCs

In monolayer TMDCs, strong Coulomb interactions due to reduced screening and strong 2D confinement lead to exceptionally high binding energies for excitons [23, 24, 36], which allow them be able to survive even at room temperature. Hence, the typical absorption spectra are usually characterized by strong excitonic peaks marked by A and B, located at 670 and 627 nm, respectively. The strong spin-orbit interaction in the valence band gives rise to a separation between them, as shown in **Figure 9**. In addition, an injection of electrons into the conduction band of MoS_2, which can be realized by gate-doping [26], photoionization of impurities [28], substrates [25] or functionalization layers [22, 27], leads to the formation of negatively charged excitons (X^-). The peak of the X^- is positioned at a lower energy side of neutral exciton with a binding energy about 36 meV for MoS_2, see the peak indicated by X^- in **Figure 10**. In addition, the emergence of the charged exciton is accompanied by a transfer of spectral weight from the exciton. Therefore, the intensity ratio between a neutral and charged exciton can be tuned externally. Besides, with increasing the nonequilibrium excess electron density, a red-shift of the excitonic ground-state absorption due to Coulomb-induced band gap shrinkage occurs. It is also worth to point out that on the one hand the trion can provide a novel channel for exciton relaxation, and on the other hand, it can also be excited by an optical phonon into an excitonic state to realize an upconversion process in monolayer WSe_2.

In the regime of high exciton density, the exciton-exciton collision leads to exciton annihilation through Auger process or formation of biexciton in the monolayer TMDCs. The biexciton is identified as a sharply defined state in the PL, see P_0 in **Figure 10** and also *XX*-peak in **Figure 11**. The nature of the biexcitonic state is supported by the dependence of its PL intensity on the excitation laser power. At low excitation laser intensity, the peaks P_0 and *X* grow superlinearly and linearly with incident laser power, whereas they increase sub-quadratically and sublinearly with the laser power at sufficiently high laser fluence. The large circular polarization of P_0 emission provides a further support for this assignment.

The polarization of the photoluminescence from the TMDCs, which is defined by $\eta = (I_{\sigma^+} - I_{\sigma^-})/(I_{\sigma^+} + I_{\sigma^-})$, inherits that of the excitation source, where I_{σ^+} (I_{σ^-}) is PL intensity of right (left) hand circularly polarized light. **Figure 11** illustrates photoluminescence spectra of monolayer WSe_2 excited by near-resonant circularly polarized radiation at 15 K. Notice that the peaks for *X*, X^-, and *XX* all exhibit significant circular polarization. In addition to biexciton emission, the *X* and X^- emission bands also exhibit strong valley polarization.

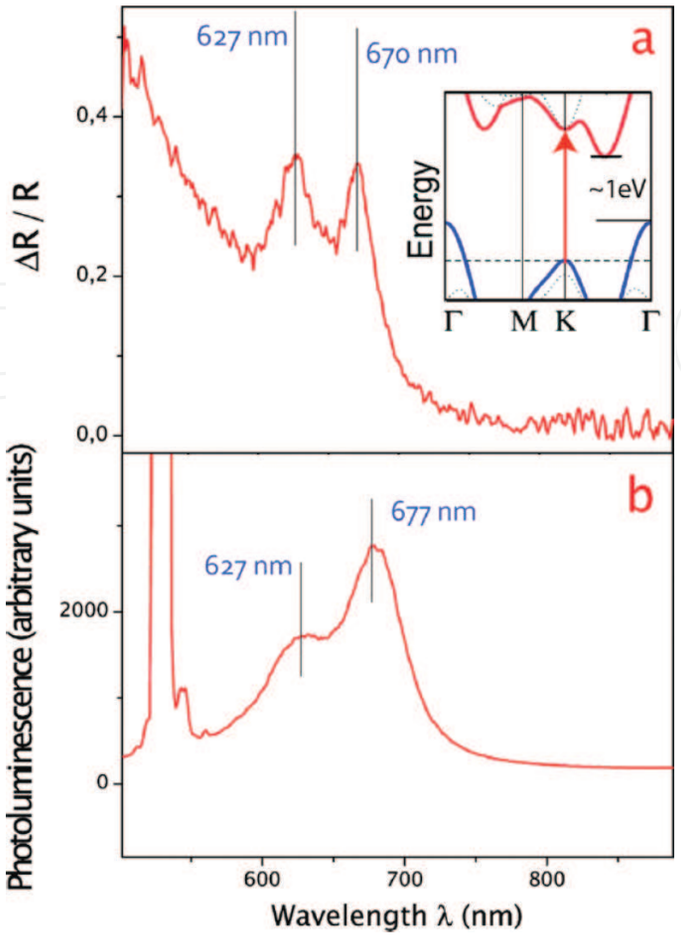

Figure 9. Reflection and photoluminescence spectra of ultrathin MoS_2 layers. (a) Reflection difference due to an ultrathin MoS_2 layer on a quartz substrate, which is proportional to the MoS_2 absorption constant. The observed absorption peaks at 1.85 eV (670 nm) and 1.98 eV (627 nm) correspond to the A and B direct excitonic transitions with the energy split from valence band spin-orbital coupling. The inset shows the bulk MoS_2 band structure neglecting the relatively weak spin-orbital coupling, which has an indirect bandgap around 1 eV and a single higher energy direct excitonic transition at the *K* point denoted by an arrow. (b) A strong photoluminescence is observed at the direct excitonic transitions energies in a monolayer, respectively [30]. (Copyright 2010 by American Chemical Society, reprinted with permission).

2.4. Defect induced photoluminescence and single photon source

As known, vacancy defects, impurities, potential wells created by structural defects or local strain or other disorders might be introduced in the growth process of the TMDC materials [12, 13, 32, 33]. They can produce localized states to participate the optical emission and absorption as manifested by P_1 to P_3 in **Figure 10**, and the emission bands on the lower energy side of the peak XX in **Figure 11**. Since the point defects can induce intervalley coupling, the defect-related emission peaks show no measurable circular polarization character. Besides, the excitons, trions, and even biexcitons can be trapped by theses crystal structure imperfections to form corresponding bound quasiparticles. Therefore, delocalized excition, charged exciton and biexciton emissions, and localized ones can coexist in the TMDCs. Interestingly, these carrier trapping centers can act as single-photon emitters to emit stable and sharp emission line [12, 13, 32, 33]. For this kind of single quantum emitter, since the maximum number of

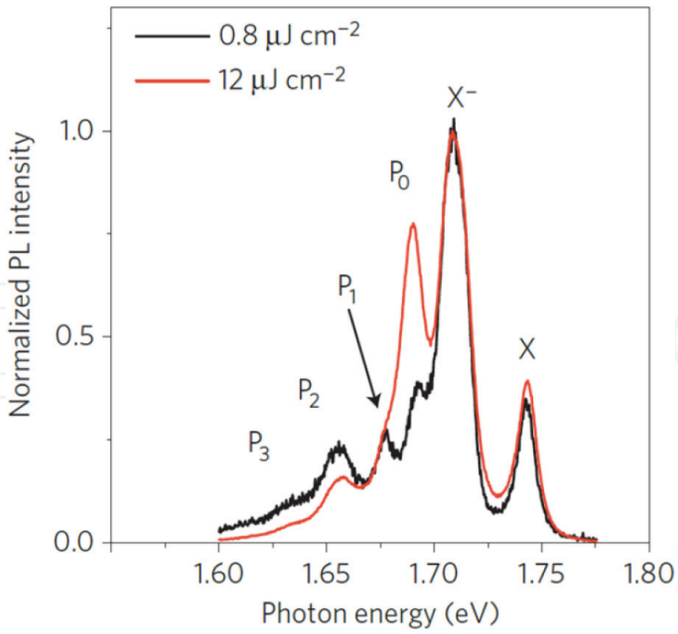

Figure 10. Photoluminescence spectra (PL) of monolayer WSe_2 at 50 K for pulsed excitation under applied pump fluences of 0.8 μJ cm^{-2} (black curve) and 12 μJ cm^{-2} (red curve), respectively. The spectra are normalized to yield the same emission strength for the neutral exciton [40]. (Copyright 2015 by the Nature Publishing Group. Reprinted with permission.)

emitted single photons is limited by the lifetime of the excited state, a saturation of the PL intensity at high excitation laser power is expected.

2.5. Magneto-optical properties of the monolayer TMDCs

The presence of a magnetic field induces a quantization of the energy levels. At high magnetic field, the Landau levels (LLs) form. The transition rate between the conduction–and valence–band Landau levels can be calculated using the eigenfunctions in Eq. 21.

$$\langle \mathbf{\Psi}_n^{\tau,+} | \mathrm{H}_{L-M}^{CP,\pm} | \mathbf{\Psi}_m^{\tau,-} \rangle = M\, \delta_{szc,szv}\, [(\tau+\sigma)\, c_{1,n}^{\tau,+}\, c_{2,m}^{\tau,-}\, \delta_{n,m+\tau} + (\tau-\sigma)\, c_{2,n}^{\tau,+}\, c_{1,m}^{\tau,-}\, \delta_{n+\tau,m}] \tag{30}$$

where

$$M = \frac{etaA_0}{2\hbar N_\tau^{n,+} N_\tau^{m,-}}. \tag{31}$$

In the presence of magnetic field, both σ^+ and σ^- absorptions take place in each valley. However, there is a great difference in their intensity. For instance, the absorption spectrum intensity of σ^+-light is 10^4 times larger than σ^--light in the K–valley. And, the lowest transition energy absorption spectrum demonstrates a valley polarization, i.e., σ^+ in the K–valley and σ^- in the K'–valley, as showed in **Figure 12** [41]. In addition, the transition occurs from $n = 0$ to $n = 1$ LLs in the K'–valley, whereas $n = 1$ to $n = 0$ LLs in the K–valley. Therefore, the valley

http://dx.doi.org/10.5772/intechopen.70300

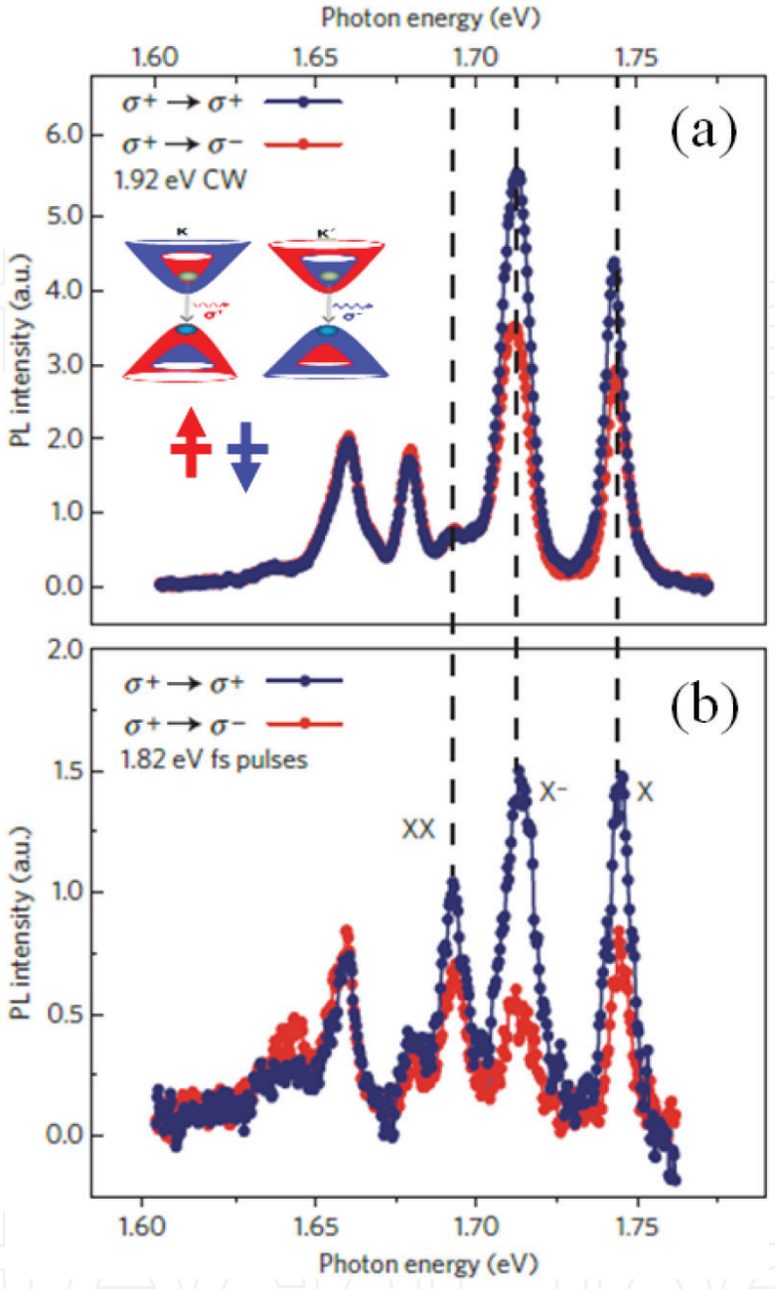

Figure 11. Circularly polarized photoluminescence (PL) spectra of monolayer WSe_2 excited by near-resonant circularly polarized radiation at 15 K. (a) PL for low exciton density with continuous wave excitation at a photon energy of 1.92 eV. (b) PL for high exciton density with pulsed excitation at a photon energy of 1.82 eV. Blue and red curves correspond to the same and opposite circularly polarized states. The emission energies for neutral (X) and charged (X^-) excitons and the biexciton (XX) state are indicated by dashed lines. Inset shows schematic diagram of energy dispersion in K- and K'-valleys and valley-polarized emission. The vertical arrows indicate the electron spin direction. The circles represent conduction and valence band electrons [40]. (Copyright 2015 by the Nature Publishing Group. Reprinted with permission).

polarization remains in the magneto-optical absorption, as showed in **Figure 13**. It is worth to argue that the higher-order terms in the effective **k**.**p** model only induces about 0.1% correction to absorption spectrum intensity [41], which allows us neglect them safely.

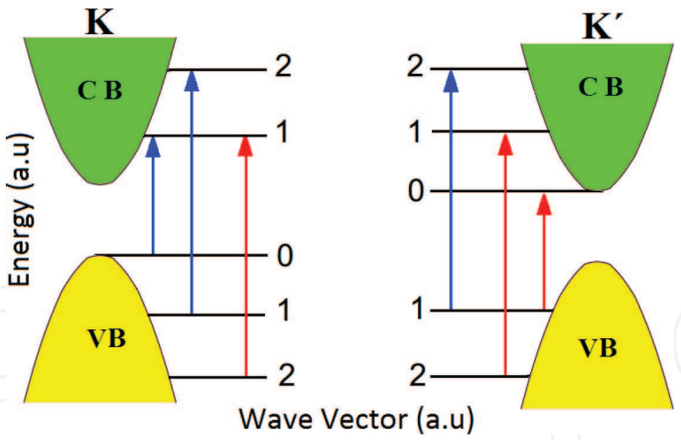

Figure 12. Selection rules for the interband transitions between Landau levels in K-valley (the left panel) and in K'-valley–valley (the right panel) of monolayer WS_2 subjected to a magnetic field along the $\hat{z}$-direction, excited by a circularly polarized light. The blue and red arrows correspond to σ^+ and σ^- absorptions, respectively [41]. (Copyright 2013 by the American Physical Society. Reprinted with permission).

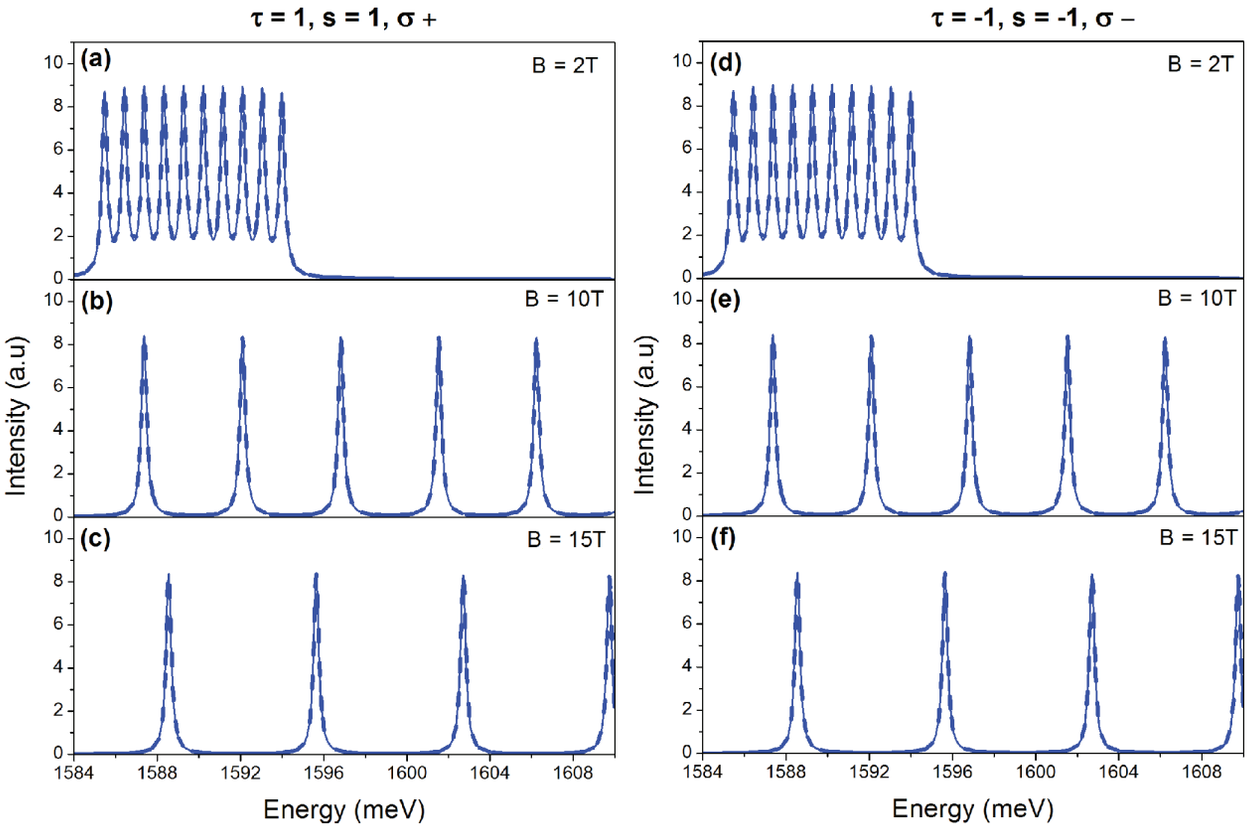

Figure 13. σ^+ absorption spectrum of monolayer MoS_2 for spin–up states in the K-valley (the left panels) and σ^- absorption spectrum for spin–down states in the K'-valley (the right panels), for a magnetic field $B = 2$ ((a) and (d)), 10 ((b) and (e)), 15T ((c) and (f)), respectively.

2.6. TMDC quantum dots and valley polarized single-photon source

The Hamiltonian of the TMDC QDs in polar coordinates is given by [15]

$$\mathrm{H} = \begin{pmatrix} \frac{\Delta}{2} & tae^{-i\tau\theta}\left(-i\tau\frac{\partial}{\partial_r} - \frac{1}{r}\frac{\partial}{\partial_\theta}\right) \\ tae^{i\tau\theta}\left(-i\tau\frac{\partial}{\partial_r} + \frac{1}{r}\frac{\partial}{\partial_\theta}\right) & -\frac{\Delta}{2} + \tau s\lambda \end{pmatrix}. \tag{32}$$

As a matter of convenience, we get rid of the angular part by using the following *ansatz* for the eigenfunctions

$$\mathbf{\Psi} = \begin{pmatrix} \psi_a(r,\theta) \\ \psi_b(r,\theta) \end{pmatrix} = \begin{pmatrix} e^{im\theta}\overline{a}(r) \\ e^{i(m+\tau)\theta}\overline{b}(r) \end{pmatrix}, \tag{33}$$

where the quantum number $m = j - \tau/2$, j is the quantum number related to the effective angular momenta $\boldsymbol{J}^{\tau}_{eff} = L_z + \hbar\tau\sigma_z/2$ with L_z being the orbital angular momenta in the $\hat{z}$ direction. Then the Schrödinger equation for TMDC QDs, showed in **Figure 14**, becomes

$$\begin{aligned} \left(\frac{\Delta}{2} - E\right)\overline{a}(r) &= ita\left(\tau\overline{b}'(r) + \overline{b}(r)\frac{(m+\tau)}{r}\right), \\ \left(\frac{\Delta}{2} - \tau s\lambda + E\right)\overline{b}(r) &= ita\left(-\tau\overline{a}'(r) + \overline{a}(r)\frac{m}{r}\right). \end{aligned} \tag{34}$$

After some algebra calculations, we get two decoupled equations. They are

$$\overline{a}''(r) + \frac{\overline{a}'(r)}{r} + \overline{a}(r)\left(\chi - \frac{m^2}{r^2}\right) = 0 \tag{35}$$

and

$$\overline{b}''(r) + \frac{\overline{b}'(r)}{r} + \overline{b}(r)\left(\chi - \frac{(m+\tau)^2}{r^2}\right) = 0 \tag{36}$$

where $\chi = \frac{(2E-\Delta)(\Delta+2E-2\lambda s\tau)}{4t^2a^2}$. These two second order differential equations can be straightforwardly resolved. Finally we obtain,

$$\overline{a}(r) = \overline{N}\left(\frac{2iat\sqrt{\chi}}{\Delta - 2E}\right)J_{|m|}(r\sqrt{\chi}) \tag{37}$$

and

$$\overline{b}(r) = \overline{N}J_{|m+\tau|}(r\sqrt{\chi}), \tag{38}$$

where $\overline{N}$ is the normalization constant and $J_n(x)$ is Bessel Function of the first kind. Applying the infinite mass boundary condition $\frac{\psi_2(R,\theta)}{\psi_1(R,\theta)} = i\tau e^{i\tau\theta}$, we obtains the secular equation

$$J_{|m+\tau|}(R\sqrt{\chi}) = -\frac{\tau(2at\sqrt{\chi})J_{|m|}(R\sqrt{\chi})}{\Delta - 2E}, \tag{39}$$

where R is the QD radius, see **Figure 14**.

From **Figures 15** and **16**, we see that the bound states formed in a single valley, and $E^{\tau}(j) \neq E^{\tau}(-j)$ for both conduction– and valence– bands. In addition, the electron-hole symmetry is broken. Due to the confinement potential, the effective time reversal symmetry (TRS) is broken within a single valley, even without the magnetic field, similarly to graphene QDs [42]. On the other hand, the inverse asymmetry of the crystalline structure, the terms of spin-orbit interaction and the confinement potential, do not commute with the effective inversion operator, defined in a single valley $P_e = I_\tau \otimes \sigma_x$. Consequently, the QDs do not preserve the electron-hole symmetry in the same valley. However, comparing **Figure 15(a, b)**, we can found that $E^{\tau}(j) = E^{-\tau}(-j)$ was still true. This is attributed to the TRS, where $THT^{-1} = H$, the TRS operator is defined as $T = i\tau_x \otimes s_y C$, with C being the conjugate complex operator.

2.7. Landau levels in monolayer MoS_2 quantum dots

Similarly to what we did in the case of the monolayer TMDCs, for quantum dot subjected to a perpendicular magnetic field, we do the Peierls substitution and use now the symmetric

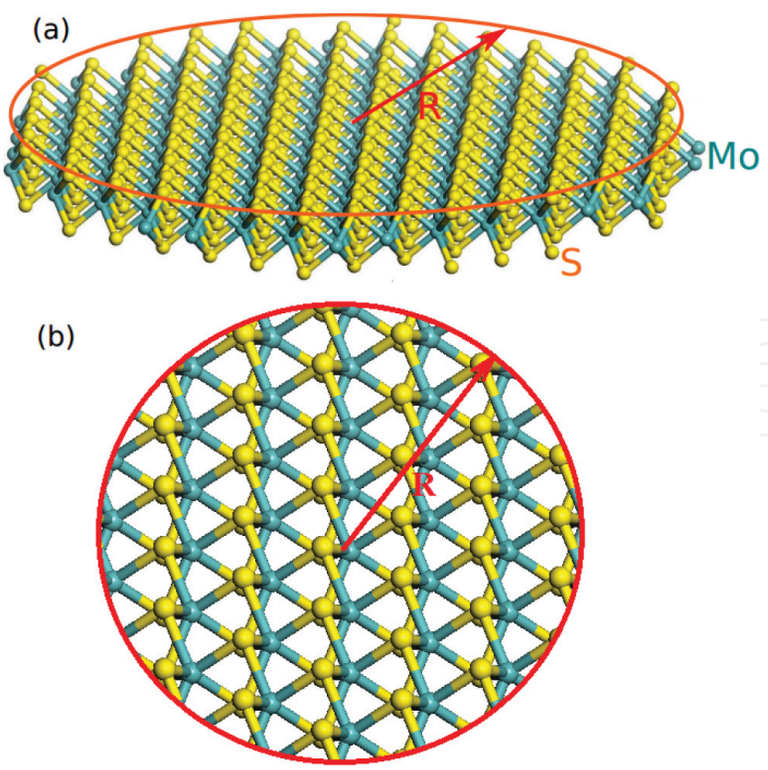

Figure 14. (a) Schematic of a monolayer MoS_2 QD with radius R. (b) Top view of MoS_2 crystal structure.

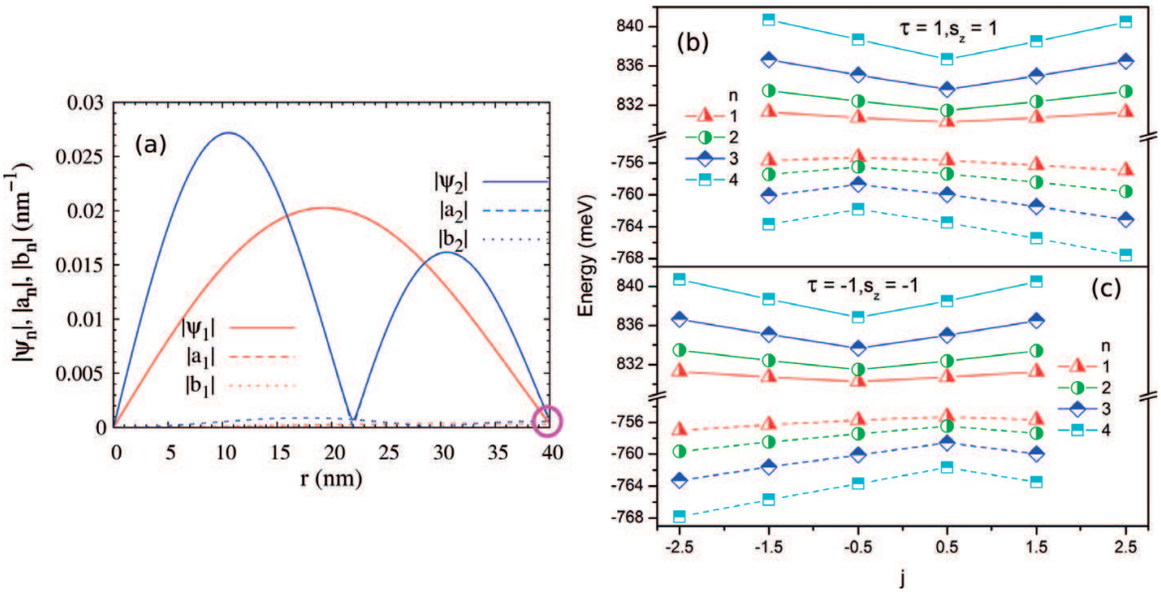

Figure 15. (a) Wave function profile Ψ_n and its two components (a_n, b_n) of the lowest two (n = 1, 2) conduction band states in the *K*–valley with spin–up at j = 1.5. The pink circle indicates that the wave function Ψ_n is nonzero (even though small) at r = R. Energy spectrum of the lowest four (n = 1, 2, 3, 4) conduction bands (solid curves) and the highest four valence bands (dashed curves) as a function of j, in the *K*-valley with spin-up (b) and *K*′-valley with spindown (c) of a MoS_2 dot. The dot size is R = 40nm and the magnetic field is B = 0 [14]. (Copyright 2016 by the IOP publishing. Reprinted with permission).

gauge, i.e., $\vec{A} = (-By/2, Bx/2)$. The part of magnetic field Hamiltonian, in polar coordinates is given by

$$\mathcal{H}_B = \begin{pmatrix} 0 & \frac{ta}{2l_B^2}\left(-ie^{-i\tau\theta}r\right) \\ \frac{ta}{2l_B^2}\left(ie^{i\tau\theta}r\right) & 0 \end{pmatrix}. \tag{40}$$

Then, the total Hamiltonian becomes $H + \mathcal{H}_B$, which leads to the following two-coupled differential equations:

$$\left(\frac{\Delta}{2} - E\right)\bar{a}(r) = iat\left(\tau\bar{b}'(r) + \bar{b}(r)\left(\frac{(m+\tau)}{r} + \frac{r}{2l_B^2}\right)\right),$$

$$\left(E + \frac{\Delta}{2} - \lambda s\tau\right)\bar{b}(r) = iat\left(-\tau\bar{a}'(r) + \bar{a}(r)\left(\frac{m}{r} + \frac{r}{2l_B^2}\right)\right). \tag{41}$$

In order to solve this eigenvalue problem, let us first decouple these two equations into

$$\bar{a}''(r) + \frac{\bar{a}'(r)}{r} + \bar{a}(r)\left(-\frac{r^2}{4l_B^4} - \kappa - \frac{m^2}{r^2}\right) = 0 \tag{42}$$

and

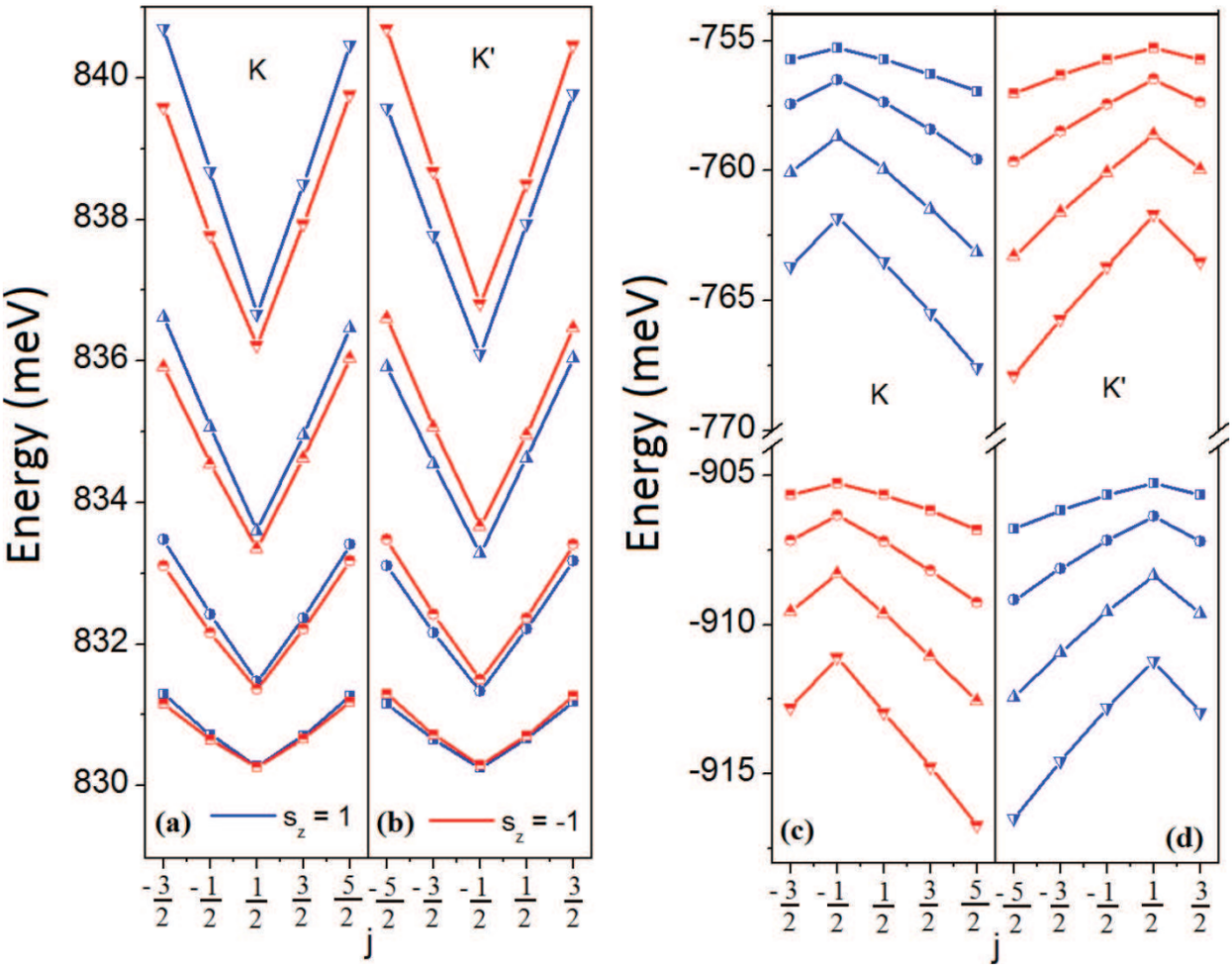

Figure 16. Energy spectrum of monolayer MoS_2 QD with a radius of 40 nm for the conduction–band in the *K*- (a) and *K*′- (b) valleys. (c) and (d) are corresponding figures for the valence–band. The blue and red curves correspond to spin–up and spin–down energy levels, respectively.

$$\overline{b}''(r) + \frac{\overline{b}'(r)}{r} + \overline{b}(r)\left(-\frac{r^2}{4l_B^4} - \phi - \frac{(m+\tau)^2}{r^2}\right) = 0 \tag{43}$$

where

$$\kappa = \frac{(m+\tau)}{l_B^2} + \frac{(\Delta - 2E)(\Delta + 2E - 2\lambda s\tau)}{4t^2a^2}, \tag{44}$$

$$\phi = \frac{m}{l_B^2} + \frac{(\Delta - 2E)(\Delta + 2E - 2\lambda s\tau)}{4t^2a^2} \tag{45}$$

Solving these equations, we obtain the following two components of the eigenfunctions

$$\overline{a}(r) = G_\xi \overline{N} r^{|m|} e^{-\frac{r^2}{4l_B^2}} {}_1F_1\left(\frac{1}{2}\left(\kappa l_B^2 + |m| + 1\right); |m| + 1; \frac{r^2}{2l_B^2}\right), \tag{46}$$

$$\overline{b}(r) = \overline{N} r^{|m+\tau|} e^{-\frac{r^2}{4l_B^2}} {}_1F_1\left(\frac{1}{2}\left(\phi l_B^2 + |m+\tau| + 1\right); |m+\tau| + 1; \frac{r^2}{2l_B^2}\right) \tag{47}$$

where

$$G_\xi = iW(\tau m)\left(\frac{4ta\left(m + \tau Q_+(\tau m)\right)}{\Delta - 2EW(\tau m) - 2\tau s\lambda Q_-(\tau m)}\right)^{W(\tau m)}, \tag{48}$$

$$W(\tau m) = S(\tau m + \varepsilon), \tag{49}$$

$$Q_\pm(\tau m) = \frac{1 \pm S(\tau m + \varepsilon)}{2}, \tag{50}$$

$S(x)$ is the sign function, ${}_1F_1(a, b, x)$ is the confluent hypergeometric function of the first kind, ε is an arbitrary constant ($0 < \varepsilon < 1$) used to avoid a singularity in the function $S(x)$.

With the eigenfunctions at hand, we can derive the secular equation for the eigenvalues by applying infinite mass boundary condition, i.e.,

$$\frac{{}_1F_1\left(\frac{1}{2}\left(\phi l_B^2 + |m+\tau| + 1\right); |m+\tau| + 1; \frac{R^2}{2l_B^2}\right)}{{}_1F_1\left(\frac{1}{2}\left(\kappa l_B^2 + |m| + 1\right); |m| + 1; \frac{R^2}{2l_B^2}\right)} = i\tau R^{|m|-|m+\tau|} G_\xi \tag{51}$$

Figure 17(a) illustrates the energy spectrum of the lowest four spinup conduction bands in the K-valley ($\tau = 1$, $s = 1$) as a function of magnetic field (B), for the orbital angular momentum $m = \pm 0, 1, \pm 2$, in the 70 nm dot. At zero magnetic field, the electronic shells of an artificial atom such as s, p, and d shells emerge. In a certain valley, say the K-valley, the atomic states possess both spin- and orbital–degeneracies such as $E(m) = E(-m)$. In addition, we should emphasize that the energy spectrum in different valleys have time reversal symmetry at $B = 0$. However, the presence of magnetic field breaks down this symmetry and leads to splittings of the atomic orbitals of the dot. Moreover, in the regime of weak magnetic fields, unlike the monolayer MoS_2 in which the energy shows linear B response, valley dependent energy levels with nonlinear B response are observed. Such effect is attributed to the competition of the QD confinement with the magnetic field effect [14].

As B increases, an effective confinement induced by the magnetic field gradually becomes comparable to that of the dot. Hence, their contributions to the electronic energy are balanced. With a further increasing of B, magnetic field effect starts to dominate the features of the energy spectrum. Accordingly, the LLs which show a linear dependence on B, became of the heavily massive Dirac character, are formed just like in the pristine monolayer MoS_2. The higher the energy level is, the stronger the magnetic field needed to form the corresponding LL. For instance, the lowest LL is formed around a critical value $B = B_c = 2T$. Interestingly, in the Hall regime, an energy locked (energy independent on B) mode referring to the lowest

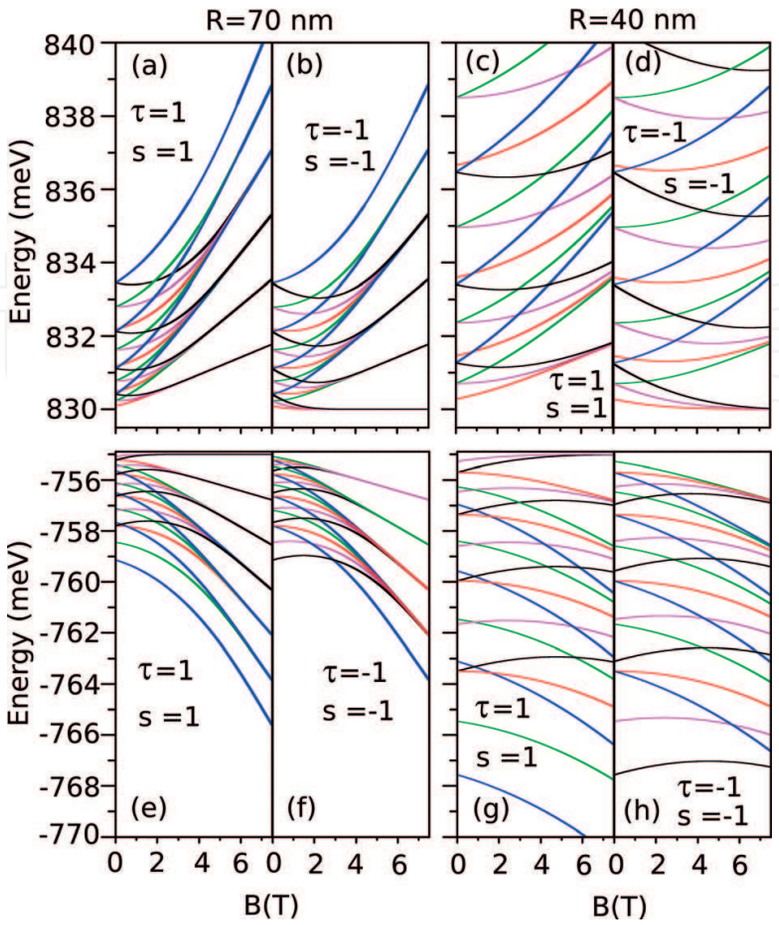

Figure 17. Energy spectrum of the lowest four conduction band states with spin–up in the *K*-valley (a) and spindown in the K'-valley (b), and the highest four valence band states with spin–up in the *K*-valley (e) and spin-down in the K'-valley (f) of a 70 nm MoS_2 QD, as a function of the magnetic field, for angular momentum $m = 0$ (red curves), -1 pink curves), 1 (green curves), -2 (black curves), and 2 (blue curves). The corresponding analogues for a 40 nm dot are shown in (c), (d), (g), and (h), respectively [14]. (Copyright 2016 by the IOP publishing. Reprinted with permission).

spin-down conduction band in the K'-valley emerges, as shown in **Figure 17(b)**. It is expected to be an analog to the zero energy mode in gapless graphene, associating with certain topological properties. These novel features of the QD energy spectrum are tunable by QD size [14].

Figure 17(c, d) are the corresponding analogs of **Figure 17(a, b)**, but for a dot with R = 40 nm. Comparing with the 70nm dot ($B_c = 2T$), here the energy locked mode takes place until $B_c = 4T$, which turns out to be larger than the one (2 T) for the 70 nm dot, indicating the locked energy modes arise from the competition between the dot confinement and the applied magnetic field [14].

Let us turn to the energy spectrum of the valence band in the dot of $R = 70nm$. **Figure 17(e, f)** show the B field dependence of the energy spectrum of the highest four valence bands for several values of angular momentum ms with $m = 0, \pm 1, \pm 2$ in the *K*-valley with spin-up ($\tau = 1, s = 1$) and K'-valley with spindown ($\tau = -1,\ s = -1$), respectively. In contrast to the conduction band, here we find $E(m) \neq E(-m)$ even at B = 0 due to the spin–orbit coupling, see **Figure 17(a, b, e, f)**. Besides that, we also observe the emergent locked energy mode around

http://dx.doi.org/10.5772/intechopen.70300

$B_c = 2T$, but referring to the highest valence band. We should emphasize that the locked energy modes for the conduction and valence bands appear in distinct valleys with opposite spin, see **Figure 17(b, e)**. The corresponding valence band energy spectra for the 40 nm dot are shown in **Figure 17(g–h)**, where the locked energy mode associated with a larger $B_c = 4T$, also arises from the combined effect of the dot confinement and the applied magnetic field, similar to the conduction band. Therefore, the flat band or energy locked modes appear only in the valence band of the K-valley and the conduction band of the K'-valley [14]. The effect of changing the magnetic field direction is showed in **Figure 19**.

A comparison of the energy spectrum of the 70 nm dot with that of the bulk TMDC (i.e., infinite geometry) is shown in **Figure 18**. Because of the large effective mass at the band edges, the LLs of the bulk TMDC scale as $E_{\pm}(\omega_c, n) = \frac{\lambda\tau s}{2} \pm \sqrt{\frac{(\Delta - \lambda\tau s)^2}{4} + t^2 a^2 \omega_c^2 n}$ in the low energy region, which resembles conventional 2D semiconductors more than Dirac fermions. The n = 0LL appears only in the conduction band of K'-valley (and the valence band of K-valley, not shown), implying the lifting of valley degeneracy for the ground state. As magnetic field increases, there is an evolution of the energy spectrum from atomic energies to Landau levels. More specifically, in the regime of weak B field, the atomic structure emerges, where the energy is distinct from that of the bulk case. On the other hand, in the strong field regime, the energy in the bulk TMDC and quantum dot becomes identical because the effective confinement due to the magnetic field dominates physical behaviors of the dot. Note that although the two band model we used here is widely adopted in the literature [39], the model itself still has limitations, e.g., it cannot properly describe the spin splitting of the conduction band, the trigonal warping of the spectrum and the degeneracy breakdown by applied magnetic field

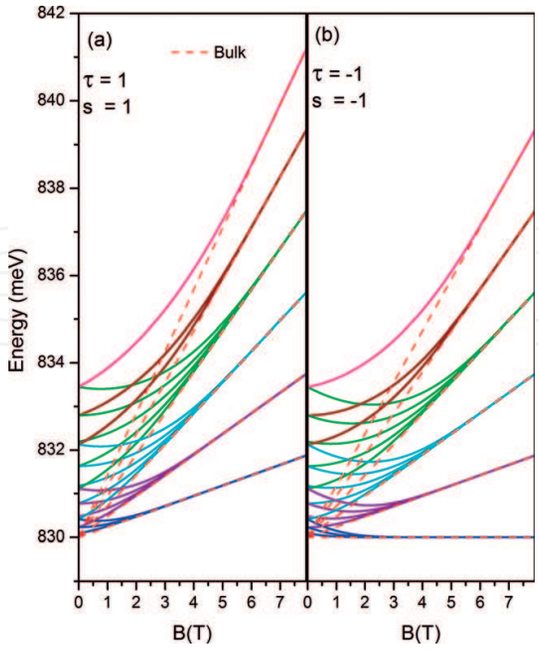

Figure 18. Energy spectrum of the conduction band states with spin–up in the K-valley (a) and spin-down in the K'-valley (b) of a monolayer MoS_2 (dotted curves) and of a MoS_2QD with radius $R = 70$ nm, as a function of the magnetic field.

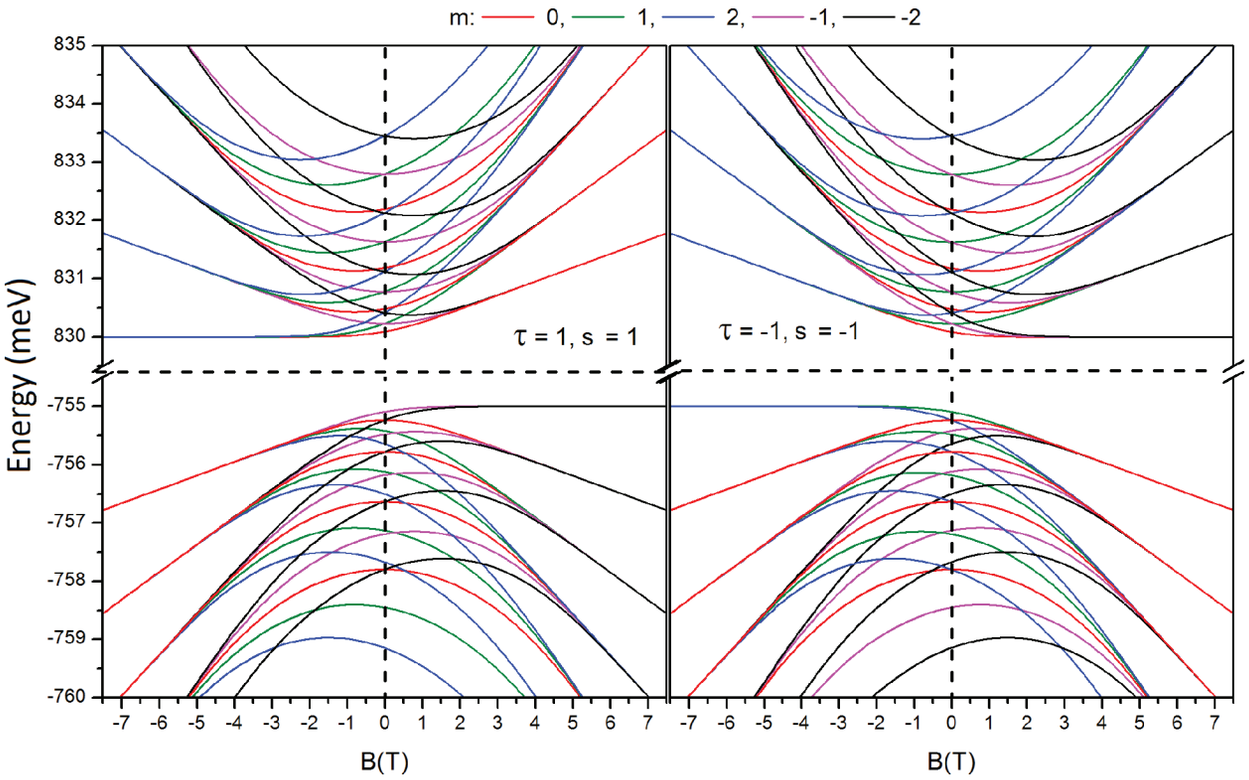

Figure 19. Energy spectrum of the states with spin-up in the K-valley (a) and spindown in the K'-valley (b) of a monolayer MoS_2 QD with radius $R = 70$ nm, as a function of the magnetic field along both positive and negative $\hat{z}$–direction, for angular momentum $m = 0$ (red curves), -1 (pink curves), 1 (green curves), -2 (black curves), and 2 (blue curves).

for Landau levels with the same quantum number. However, for usual experimental setups, these effects in the vicinity of the K or K' valley in which we are interested play a minor role. Hence it can be safely neglected.

2.8. Optical selection rules in monolayer MoS_2 quantum dots

In the QDs as demonstrated in **Figure 20**, the optical transition matrix elements in the QDs are computed by,

$$\langle \mathbf{\Psi}_c | \mathcal{H}_{L-M} | \mathbf{\Psi}_v \rangle = \left(\frac{\pi A_0}{\hbar} \right) \delta_{s_{zv}, s_{zc}} [(\tau - \sigma)\delta_{m_v, m_c + \tau} R_{-\sigma} + (\tau + \sigma)\delta_{m_c, m_v + \tau} R_{\sigma})], \tag{52}$$

where s_{zv} (s_{zc}) denote the valence (conduction) band spin state, $R_{-\sigma} = \int_0^R b_c^* a_v r dr$ and $R_{\sigma} = \int_0^R a_c^* b_v r dr$ with $a_{c/v}$ and $b_{c/v}$ the radial components of the conduction/valence band spinor. The selection rule for optical transitions in TMDC QDs is defined by $m_v - m_c = \pm\tau$ and $s_{zv} = s_{zc}$, i.e., the angular momentum of the initial and final states differs by ± 1, but the spin of these two states is the same. The magnitude of transition rates is determined by the integral $R_{-\sigma}$ and R_{σ} for the transitions taking place in the valley $\tau = -\sigma$ and σ, respectively. Since $|a_c(r)| > |b_c(r)|$ and $|a_v(r)| < |b_v(r)|$, the integral $R_{-\sigma}$ is much smaller than the R_{σ}. As a

http://dx.doi.org/10.5772/intechopen.70300

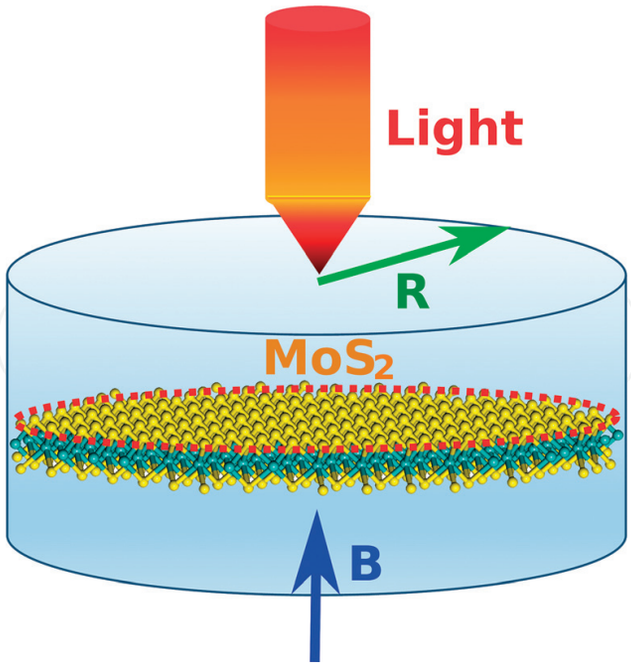

Figure 20. Schematic of a monolayer MoS_2 circular quantum dot with radius R indicated by a red circle, excited by a light field. A magnetic field B is applied perpendicularly to the MoS_2 sheet [15]. (Copyright 2017 by the Nature Publishing Group. Reprinted with permission).

consequence, the absorption in the valley $\tau = \sigma$ is stronger than that in the $\tau = -\sigma$, which leads to a valley selected absorption. In a special case in which one component of the wave function spinor is equal to zero such as $n_{ll} = 0$ LL, only photons with the helicity $\sigma = \tau$ is absorbed. Then, one obtains a dichroism $\eta = 1$. For the linear polarized light, however, there is no valley polarization in the absorption spectrum, in contrast to the case of CPL [15].

In the 2D bulk MoS_2, the bottom of the conduction band at the two valleys is characterized by the orbital angular momentum $m = 0$. In contrast, at the top of the valence band, the orbitals with $m = 2$ in the K-valley, whereas m is equal to -2 in the K'-valley. The valley dependent angular momentum in the valence band allows one to address different valleys by controlling the photon angular momentum, i.e., the helicity of the CP light. Such valley-specific circular dichroism of interband transitions in the 2D bulk has been confirmed [19, 43, 44]. The question is whether its counterpart QD also possesses this exotic optical property. **Figure 21(a, b)** depict zero-field band-edge optical absorption spectrum of a 70-nm dot pumped by the CP light field. Interestingly, one notices that (i) the polarization of the absorption spectrum is locked with the valley degree of freedom, manifested by the intensity of absorption spectrum with $\sigma = \tau$ being about 106 times stronger than that with $\sigma = \tau$, and (ii) the spectrum is spin-polarized. Thus, the QDs indeed inherit the valley and spin dependent optical selection rule from their counterpart of 2D bulk MoS_2. In spite of the distinction in the spin- and valley-polarization of absorption spectra in the distinct valleys, their patterns are the same required by the time reversal symmetry. In **Figure 21(c, f)** we show the zero-field optical absorption spectrum as a function of excitation energy for several values of dot-radius within R = 20–80 nm. The involved transitions in **Figure 21(c, f)** lagged by the numbers have been schematically illustrated in **Figure 21(g)**. Alike conventional semiconductor QDs, several peaks stemmed from discrete excitations of

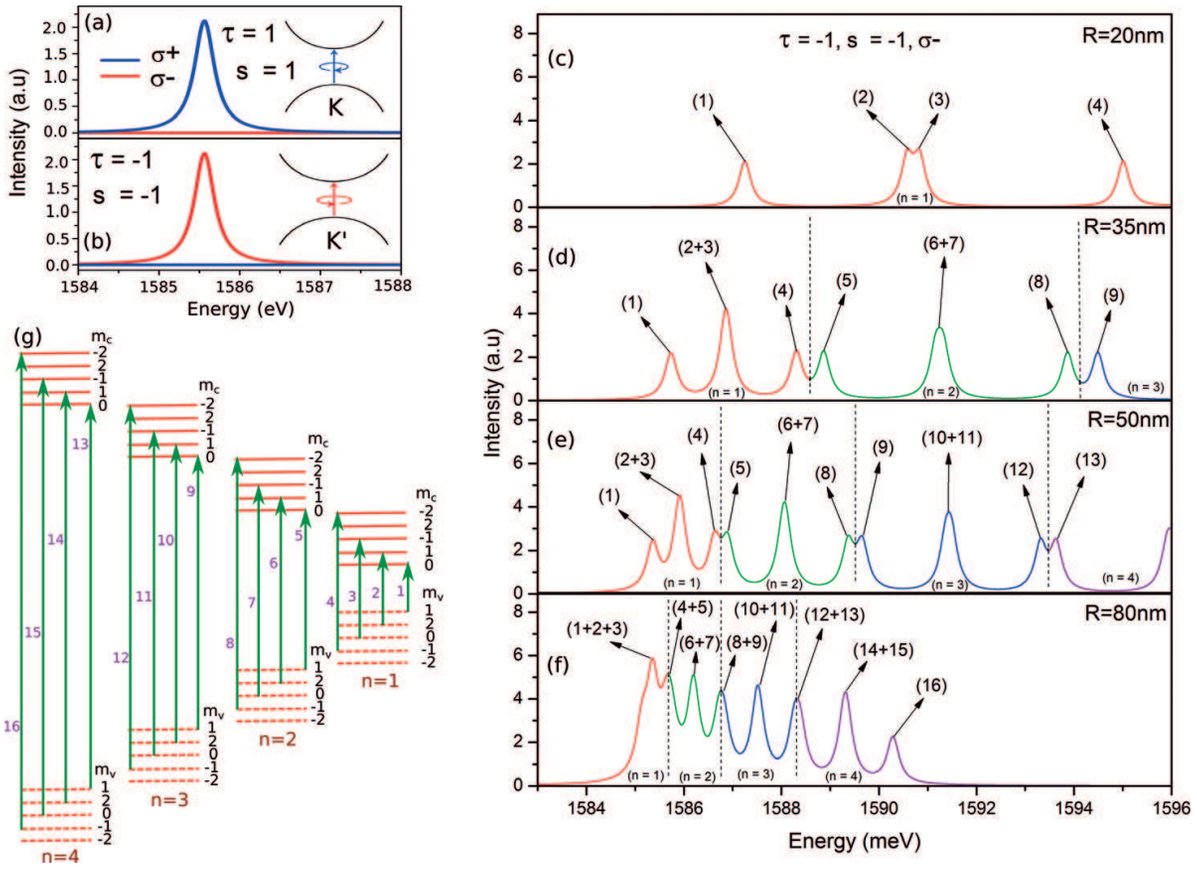

Figure 21. Zero-field optical absorption spectrum associated with interband transitions between conduction and valence-band ground states of a 70-nm MoS_2 dot for the spin-up state in the *K*-valley (a) and for the spin-down state in the *K*′-valley (b), pumped by both clockwise (σ^+, blue curve) and anticlockwise (σ^-, red curve) circularly polarized light fields. (c–f) Absorption intensity for the spin-down state in the *K*′-valley under the excitation of σ^-, for QDs of R = 20, 35, 50, and 80 nm, respectively. (g) Schematic diagram of the involved interband transitions in (c-f) tagged by the numbers. The color of the curves is used to highlight the principle quantum number (n) of transition involved states [15]. (Copyright 2015 by the Nature Publishing Group. Reprinted with permission).

the MoS_2 QD are observed. As the dot size decreases, the peaks of absorption spectrum undergo a blue shift. In other words, a reduction of the dot size pushes the electron excitations to take place between higher energy states, as a result of the enhancement of the confinement on carriers induced by a shrink of the dot. Therefore, the spin-coupled valley selective absorption with a tunable transition frequency can be achieved in QDs by varying dot geometry, in contrast to the 2D bulk where a fixed transition frequency is uniquely determined by the bulk band structure. In addition to the blue shift of the transition frequency, the absorption intensity can also be controlled by dot geometry due to size dependence of the peak interval. In fact, an increasing of dot size results in a reduction of the energy separation among confined states. Thus, as the dot size increases, the absorption peaks get closer and closer, see **Figure 21(c–f)**. Eventually, several individual absorption peaks merge together to yield a single composite-peak with an enhanced intensity. For instance, for the 20-nm dot (**Figure 21c**), the lowest energy peak is generated by only one transition, labeled by (1) (see also **Figure 21g**). However, for the dot with R = 80nm, we observe a highly enhanced absorption intensity labeled by

$(1+2+3)$, which in the 20-nm dot refers to three separated peaks with weak absorption intensities indicated by (1), (2), (3), respectively.

2.9. Magneto-optical properties of monolayer MoS_2 quantum dots

With the knowledge of the energy spectrum and eigenfunctions of the QD, we are ready to study its magneto-optical properties. The optical transition matrix in Eq. 27 is applicable to the current case provided that we use newly obtained wavefunctions presented in Eq. 47 and Eq. 48.

Figure 22 shows the magneto-optical absorption spectra for the spin-down states in the K'-valley of a monolayer MoS_2 QD with $R = 40$ nm excited by left-hand circularly polarized

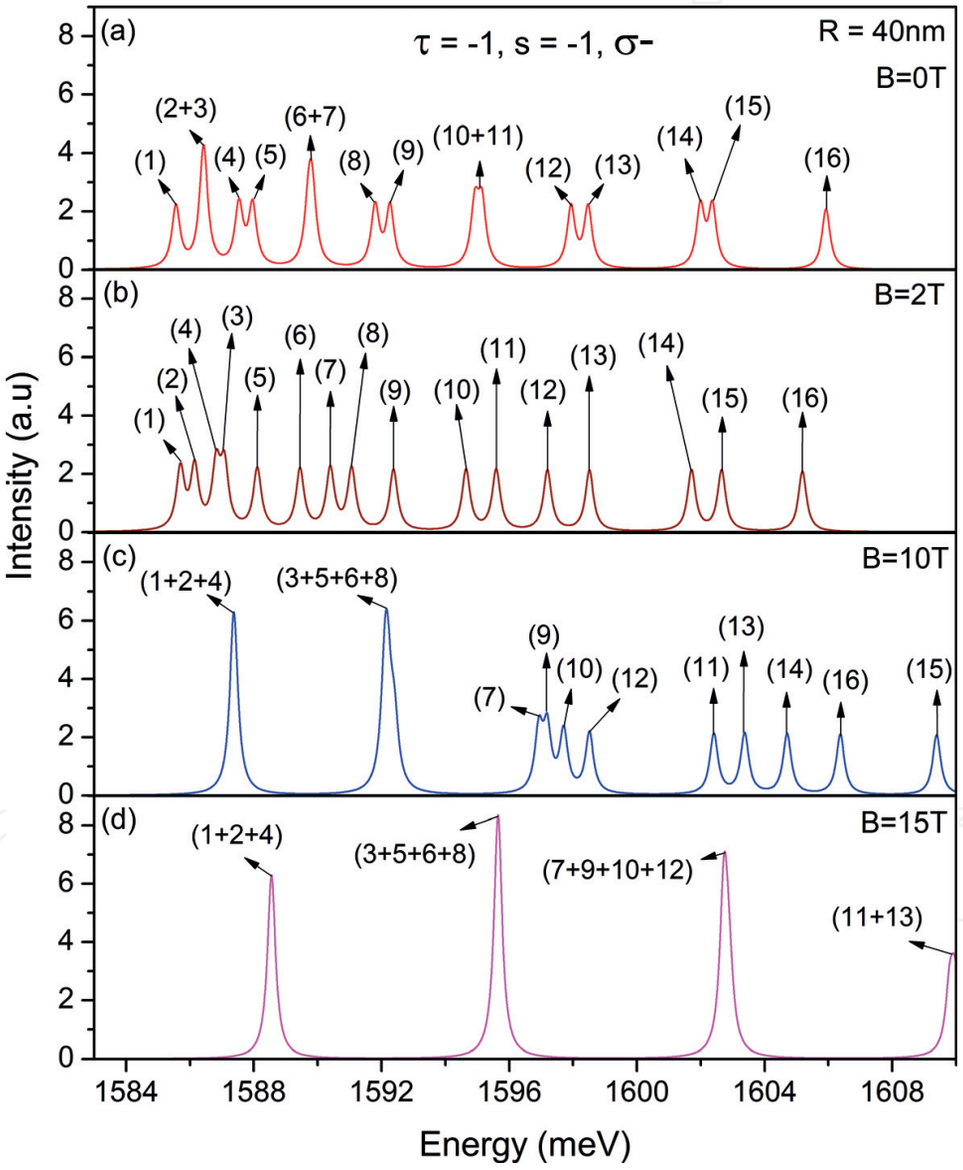

Figure 22. Absorption spectrum for the spin-down states in the K'-valley of a monolayer MoS_2 QD with $R = 40$ nm excited by left-hand circularly polarized light σ^-, at the magnetic field $B = 0$ (a), 2T (b), 10T (c), 15T (d), respectively. The corresponding enumerated optical transitions are schematically shown in **Figure 21(g)** [15]. (Copyright 2015 by the Nature Publishing Group. Reprinted with permission).

light σ^-, for several values of magnetic field ranging from 0 to 15 T. A few interesting features are observed. Firstly, the magneto-optical absorption is also spin- and valley-dependent, as it does in optical absorption spectrum at zero field. In particular the lowest transition energy absorption peak related to the interband transition involving $n_{ll} = 0$ LL is totally valley polarized with dichroism equal to 1. Thus, the polarization of magneto-optical absorption locks with the valley. Secondly, for a fixed value of dot size, increasing (decreasing) the strength of the magnetic field results in a blue (red) shift in the absorption spectrum. This arises from the fact that the magnetic field induces an effective confinement characterized by the magnetic length $l_B = \sqrt{\hbar/eB}$, which is more pronounced for a stronger magnetic field. In addition, the magnetic quantization induced by the magnetic field favors the QD to absorb photons with higher energies. The stronger the magnetic field, the greater the capacity of the QDs to absorb the photons of higher energy. Thirdly, in the high magnetic-field regime the absorption intensity can be highly enhanced by increasing the strength of magnetic field due to increased degeneracy of the LLs.

2.10. Excitonic effect in monolayer MoS_2 quantum dots

The optical and magneto-optical absorptions that we have discussed so far are based on the independent electron-hole picture. In reality, there is a strong Coulomb interaction between the electron and hole in MoS_2. The full treatment of the Coulomb interaction using many-body theory is beyond the scope of this chapter. However, the excitonic effects in absorption spectrum of the monolayer MoS_2 QDs can be properly addressed by an exact diagonalization, which is adopted in this work. The Hamiltonian used to describe the exciton is, $H(\mathbf{r}_\mathrm{e}, \mathbf{r}_\mathrm{h}) = \mathcal{H}_\mathrm{e}(\mathbf{r}_\mathrm{e}) + \mathcal{H}_\mathrm{h}(\mathbf{r}_\mathrm{h}) + V^{\mathrm{e-h}}(\mathbf{r}_\mathrm{e} - \mathbf{r}_\mathrm{h})$, where $\mathcal{H}_{\mathrm{e(h)}}$ is the single electron (hole) Hamiltonian in QDs (see Eq. 1) and $V^{\mathrm{e-h}}$ is the electron-hole Coulomb interaction given by $V^{\mathrm{e-h}}(|\mathbf{r}_\mathrm{e} - \mathbf{r}_\mathrm{h}|) = (1/4\pi\epsilon_r\epsilon_0)(e^2/|\mathbf{r}_\mathrm{e} - \mathbf{r}_\mathrm{h}|)$. Here ϵ_0 is the permittivity, ϵ_r is the dielectric constant, and $\mathbf{r}_e$ and $\mathbf{r}_h$ respectively stand for the position of electron and hole. An exciton can be understood as a coherent combination of electron-hole pairs. Thus, the wavefunctions of an exciton can be constructed based on a direct product of single-particle wave functions for the electron and hole. Since the electron-hole Coulomb interaction is larger than or at least in the same magnitude as the quantum confinement in the MoS_2 QDs, the excitonic effect play an very important role. Hence the single-particle wavefunctions should be modified due to the presence of the Coulomb interaction. Therefore, to get quick convergence of numerical calculation, instead of using simple single-particle wavefunction, we use the modified one to construct the exciton states, i.e., $\chi_j(r_{e,h}) = N \exp(-r_{e,h}/r_b)\mathbf{\Psi}_j(r_{e,h})$, where the exponential factor is a hydrogen-like s-wave state, N is the normalization constant, $\mathbf{\Psi}_j$ is the wave function of the Hamiltonian $\mathcal{H}_{\mathrm{e,h}}$, and r_b is the exciton bohr radius, which has the value of $r_b \sim 1$ nm in MoS_2 [24]. Then, the exciton wave function $\mathbf{\Psi}_{exc}$ can be straightforwardly written as,

$$\mathbf{\Psi}^{\nu}_{exc}(\mathrm{r}_\mathrm{e}, \mathrm{r}_\mathrm{h}) = \sum_{i,j} C^{\nu}_{i,j}\ \chi_i(\mathrm{r}_\mathrm{e})\ \chi_j(\mathrm{r}_\mathrm{h}), \tag{54}$$

with the superscript ν referring to the ν-th exciton state. Within the Hilbert space made of states of electron-hole pairs $\{\chi_i(\mathbf{r}_e)\chi_j(\mathbf{r}_h)\}$, the matrix element of Coulomb integral reads,

$$V^{e-h}_{prsq} = -\frac{e^2}{4\pi\epsilon_0\epsilon_r}\iint \frac{\chi^*_p(\mathrm{r}_e)\chi^*_r(\mathrm{r}_h)\chi_s(\mathrm{r}_h)\chi_q(\mathrm{r}_e)}{|\mathrm{r}_e - \mathrm{r}_h|} d\mathrm{r}_e d\mathrm{r}_h, \tag{55}$$

which involves the wave function χ_i of the electron and hole in the absence of Coulomb interaction, with $j = p, r, s, q$ indicating the state index. We should emphasize that Eq. 55 contains both the direct interaction between the electron and hole, i.e., Eq. 55 at $p = q$ and $r = s$,

$$V^{e-h,dir}_{prrp} = -\frac{e^2}{4\pi\epsilon_0\epsilon_r}\iint \frac{|\chi_p(\mathrm{r}_e)|^2|\chi_r(\mathrm{r}_h)|^2}{|\mathrm{r}_e - \mathrm{r}_h|} d\mathrm{r}_e d\mathrm{r}_h, \tag{56}$$

and the exchange interaction, i.e., Eq. 55 at $s = p$ and $r = q$,

$$V^{e-h,ex}_{prpr} = -\frac{e^2}{4\pi\epsilon_0\epsilon_r}\iint \frac{\chi^*_p(\mathrm{r}_e)\chi^*_r(\mathrm{r}_h)\chi_p(\mathrm{r}_h)\chi_r(\mathrm{r}_e)}{|\mathrm{r}_e - \mathrm{r}_h|} d\mathrm{r}_e d\mathrm{r}_h. \tag{57}$$

To calculate Coulomb interaction defined in Eq. 55, we expand $1/|\mathbf{r}_e - \mathbf{r}_h|$ in terms of half-integer Legendre function of the second kind $Q_{m-1/2}$, i.e.,

$$\frac{1}{|\mathbf{r}_e - \mathbf{r}_h|} = \frac{1}{\pi\sqrt{r_e r_h}}\sum_{m=0}^{\infty}\epsilon_m \cos\left[m(\theta_e - \theta_h)\right] Q_{m-1/2}(\xi), \tag{58}$$

which is widely used in many-body calculations [45]. Here $\theta_{e(h)}$ is the polar angle of the position vector $\mathbf{r}_{e(h)}$ in the 2D plane of MoS_2, $\xi = (r_e^2 + r_h^2)/2r_e r_h$, $\epsilon_m = 1$ for $m = 0$ and $\epsilon_m = 2$ for $m \neq 0$. The exciton energy and the corresponding wavefunction can be obtained by diagonalization of the matrix of many-particle Hamiltonian $H(\mathbf{r}_e, \mathbf{r}_h)$. With the exciton state at hand (Eq. 54), we are ready to the determine the excitonic absorption involving a transition from the ground state $|0\rangle$ to exciton state $|f\rangle = |\Psi_{exc}\rangle$,

$$A(\omega) = \sum_f |\langle 0\mathcal{P}|f\rangle|\ \delta\{\hbar\omega - E^{\nu}_{exc}\}, \tag{59}$$

where E^{ν}_{exc} and $\hbar\omega$ are the exciton- and photon-energy, respectively, and $\mathcal{P} = \sum_{i,j}\delta_{sz,sz'}\langle\chi_i|\mathcal{H}_{L-M}|\chi_j\rangle\ a_{i,sz}\ h_{j,sz'}$ is the polarization operator, with $a_{i,sz}$ and $h_{j,sz'}$ being the electron and hole annihilation operators. After straightforward calculation, we finally obtain

$$A(\omega) = \sum_{\nu}\left(\delta_{sz,sz'}\sum_{i,j}C^{\nu}_{i,j}\langle\chi_i|\mathcal{H}_{L-M}|\chi_j\rangle\right)\delta\{\hbar\omega - E^{\nu}_{exc}\}. \tag{60}$$

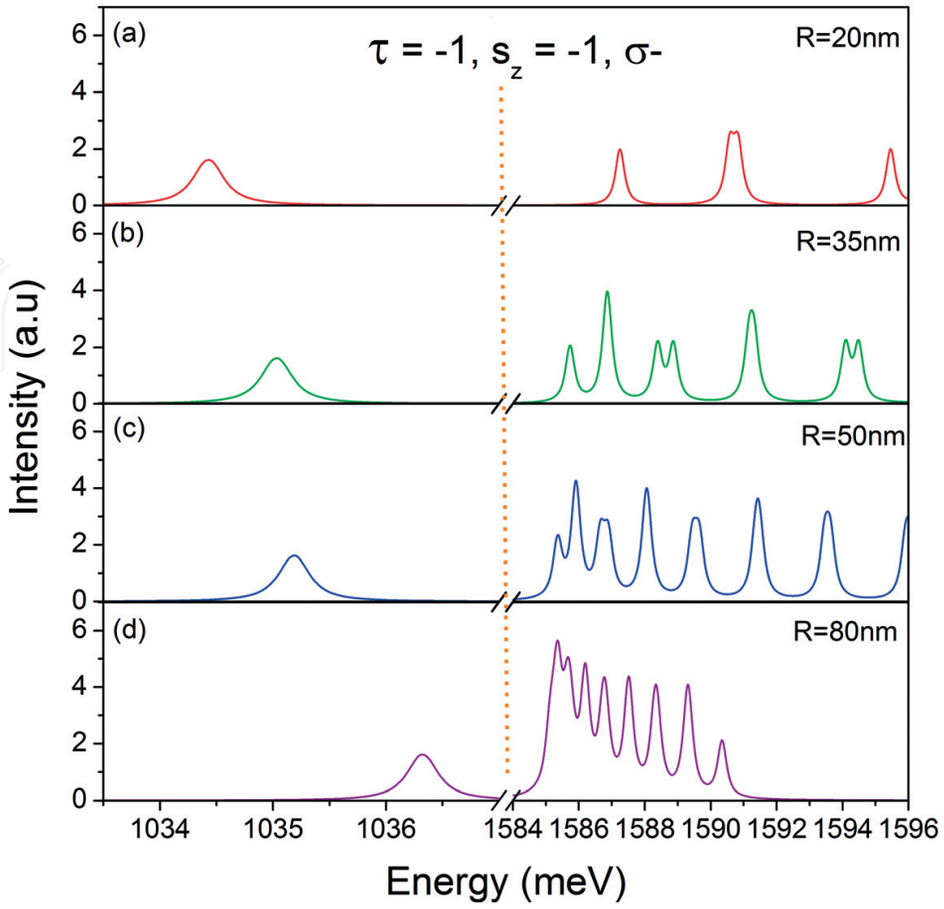

Figure 23. Excitonic effects on zero-field optical absorption spectra for the spin-down states in the K'-valley of monolayer MoS_2 QD with R = 20 nm (a), 35 nm (b), 50 nm (c), and 80 nm (d) under the excitation of the left-hand circularly polarized light σ^-. The Fermi energy is chosen as 0. The vertical dashed line separates two distinct regions of the absorption spectrum: left-hand side for excitonic absorption and right-hand side for single-particle like absorption. To be consistent with the experimental report of excitonic absorption energy, a right shift of photon energy of 700 meV is made [15]. (Copyright 2015 by the Nature Publishing Group. Reprinted with permission.)

In our numerical calculations, we have used five modified single-particle basis functions with angular momentum ranging from −2.5 to 1.5. **Figure 23** shows that there is an exciton absorption peak located at around 550 meV (i.e., exciton binding energy) below the band-edge absorption. And, the excitonic absorption peak shifts monotonically to higher absorption energy as the dot size is increased. Above the band gap, however, the spectrum is similar to what we found in previous sections in the band-to-band transitions using the independent electron-hole model. Since the exciton absorption peak is far away from the band-edge absorption, one can in principle study them separately. And, the Coulomb interaction between electron-hole pair does not change the valley selectivity and our general conclusion. Finally, it is worth to remarking that one can shift the excitonic absorption peak to a higher absorption energy, by varying the band gap parameter (Δ) in our model Hamiltonian.

Author details

Fanyao Qu[1]*, Alexandre Cavalheiro Dias[1], Antonio Luciano de Almeida Fonseca[1], Marco Cezar Barbosa Fernandes[1] and Xiangmu Kong[2]

*Address all correspondence to: fanyao@unb.br

1 Institute of Physics, University of Brasília, Brazil

2 Department of Physics, Qu Fu Normal University, China

References

[1] Reimann SM, Manninen M. Reviews of Modern Physics. 2002;**74**:1283

[2] Kuwenhoven LP, Austing DG, Tarucha S. Reports on Progress in Physics. 2001;**64**:701

[3] Heinrich AJ, Gupta JA, Lutz CP, Eigler DM. Science. 2004;**306**:466

[4] Qu F, Hawrylak P. Physical Reviews Letters. 2005;**95**:217206

[5] Qu F, Hawrylak P. Physical Reviews Letters. 2006;**96**:157201

[6] Besombes L, Léger Y, Maingault L, Ferrand D, Mariette H, Cibert J. Physical Reviews Letters. 2004;**93**:207403

[7] Léger Y, Besombes L, Maingault L, Ferrand D, Mariette H. Physical Reviews Letters. 2005;**95**:047403

[8] Gould C, Slobodskyy A, Supp D, Slobodskyy T, Grabs P, Hawrylak P, Qu F, Schmidt G, Molenkamp LW. Physical Reviews Letters. 2006;**97**:017202

[9] Villegas-Lelovsky L, Qu F, Massa LO, Lopez-Richard V, Marques GE. Physical Review B. 2011;**84**:075319

[10] Qu F, Villegas-Lelovsky L, Morais PC. Physical Review B. 2015;**92**:115445

[11] Li X, Rui M, Song J, Shen Z, Zeng H. Advanced Functional Materials. 2015;**25**:4929

[12] Srivastava A, Sidler M, Allain AV, Lembke DS, Kis A, Imamolu A. Nature Nanotechnology. 2015;**10**:491

[13] Pavlovi S, Peeters FM. Physical Review B. 2015;**91**:155410

[14] Dias AC, Fu J, Villegas-Lelovsky L, Qu F. Journal of Physics: Condensed Matter. 2016; **28**:375803

[15] Qu F, Dias AC, Fu J, Villegas-Lelovsky L, Azevedo DL. Scientific Reports. 2017;**7**:41044

[16] Castro Neto AH, Guinea F, Peres NMR, Novoselov KS, Geim AK. Reviews of Modern Physics. 2009;**81**:109

[17] Alessandro M, Joshua G, Houssa M, Xu Y, Zhang SC, Akinwande D. Journal of Nanomaterials. 2017;**16**:163

[18] Balendhran S, Walia S, Nili H, Sriram S, Bhaskaran M. Small 2015;**11**:633

[19] Xiao D, Liu GB, Feng W, Xu X, Yao W. Physical Reviews Letters. 2012;**108**:196802

[20] Song XX, Liu D, Mosallanejad V, You J, Han TY, Chen DT, Li HO, Cao G, Xiao M, Guo GC, Guo GP. Nanoscale. 2015;**7**:16867

[21] Chernikov A, van der Zande AM, Hill HM, Rigosi AF, Velauthapillai A, Hone J, Heinz TF. Physical Reviews Letters. 2015;**115**:126802

[22] Withers F, Del Pozo-Zamudio O, Mishchenko A, Rooney AP, Gholinia A, Watanabe K, Taniguchi T, Haigh SJ, Geim AK, Tartakovskii AI, Novoselov KS. Nature Materials. 2015; **14**:301

[23] Bellus MZ, Ceballos F, Chiu HY, Zhao H. ACS Nano. 2015;**9**:6459

[24] Mak KF, He K, Lee C, Lee GH, Hone J, Heinz TF, Shan J. Nature Materials. 2013;**12**:207

[25] Li Y, Qi Z, Liu M, Wang Y, Cheng X, Zhang G, Sheng L. Nanoscale. 2014;**6**:15248

[26] Lin JD, Han C, Wang F, Wang R, Xiang D, Qin S, Zhang XA, Wang L, Zhang H, Wee ATS, Chen W. ACS Nano. 2014;**8**:5323

[27] Lin Y, Ling X, Yu L, Huang S, Hsu AL, Lee YH, Kong J, Dresselhaus MS, Palacios T. Nano Letters. 2014;**14**:5569

[28] Zhang C, Wang H, Chan W, Manolatou C, Rana F. Physical Review B. 2014;**89**:205436

[29] Padilha JE, Peelaers H, Janotti A, Van de Walle CG. Physical Review B. 2014;**90**:205420

[30] Splendiani A, Sun L, Zhang Y, Li T, Kim J, Chim CY, Galli G, Wang F. Nano Letters. 2010; **10**:1271

[31] Heo H, Sung JH, Cha S, Jang BG, Kim JY, Jin G, Lee D, Ahn JH, Lee MJ, Shim JH, Choi HY, Jo MH. Nature Communications. 2015;**6**:7372

[32] Koperski M, Nogajewski K, Arora A, Cherkez V, Mallet P, Veuillen JY, Marcus J, Kossacki P, Potemski M. Nature Nanotechnology. 2015;**10**:503

[33] He YM, Clark G, Schaibley JR, He Y, Chen MC, Wei YJ, Ding X, Zhang Q, Yao W, Xu X, Lu JW, Lu CY, Pan JW. Nature Nanotechnology. 2015;**10**:497

[34] Sheng YB, Zhou L, Zhao SM, Zheng BY. Physical Review A. 2012;**85**:012307

[35] Gl AD, Potasz P, Hawrylak P. Graphene-Based Integrated Electronic, Photonic and Spintronic Circuitin Future Trends in Microelectronics: Frontiers and Innovations. Luryi S, Xu J, Zaslavsky A, editors. Wiley-IEEE Press; 2013. ISBN: 978-1-118-44216-6

[36] Wu F, Qu F, MacDonald AH. Physical Review B. 2015;**91**:075310

[37] Chakraborty C, Kinnischtzke L, Goodfellow KM, Beams R, Vamivakas AN. Nature Nanotechnology. 2015;**10**:507

[38] Lwdin PO. International Journal of Quantum Chemistry. 1982;**21**:69

[39] Liu GB, Shan WY, Yao Y, Yao W, Xiao D. Physical Review B. 2013;**88**:085433

[40] You Y, Zhang XX, Berkelbach TC, Hybertsen MS, Reichman DR, Heinz TF. Nature Physics. 2015;**11**:477

[41] Rose F, Goerbig MO, Piechon F. Physical Review B. 2013;**88**:125438

[42] Recher P, Trauzettel B, Rycerz A, Blanter YM, Beenakker CWJ, Morpurgo AF. Physical Review B. 2007;**76**:235404

[43] Mak KF, He K, Shan J, Heinz TF. Nature Nanotechnology. 2012;**7**:494

[44] Cao T, Wang G, Han W, Ye H, Zhu C, Shi J, Niu Q, Tan P, Wang E, Liu B, Feng J. Nature Communications. 2012;**3**:887

[45] Cohl HS, Rau ARP, Tohline JE, Browne DA, Cazes JE, Barnes EI. Physical Review A. 2001;**64**:052509

IntechOpen